Eddy Generation and Jet Formation via Dense Water Outflows across the Antarctic Continental Slope

ANDREW L. STEWART

Department of Atmospheric and Oceanic Sciences, University of California, Los Angeles, Los Angeles, California

ANDREW F. THOMPSON

Environmental Sciences and Engineering, California Institute of Technology, Pasadena, California

(Manuscript received 15 June 2016, in final form 21 September 2016)

ABSTRACT

Along various stretches of the Antarctic margins, dense Antarctic Bottom Water (AABW) escapes its formation sites and descends the continental slope. This export necessarily raises the isopycnals associated with lighter density classes over the continental slope, resulting in density surfaces that connect the near-freezing waters of the continental shelf to the much warmer circumpolar deep water (CDW) at middepth offshore. In this article, an eddy-resolving process model is used to explore the possibility that AABW export enhances shoreward heat transport by creating a pathway for CDW to access the continental shelf without doing any work against buoyancy forces. In the absence of a net alongshore pressure gradient, the shoreward CDW transport is effected entirely by mesoscale and submesoscale eddy transfer. Eddies are generated partly by instabilities at the pycnocline, sourcing their energy from the alongshore wind stress, but primarily by instabilities at the CDW–AABW interface, sourcing their energy from buoyancy loss on the continental shelf. This combination of processes induces a vertical convergence of eddy kinetic energy and alongshore momentum into the middepth CDW layer, sustaining a local maximum in the eddy kinetic energy over the slope and balancing the Coriolis force associated with the shoreward CDW transport. The resulting slope turbulence self-organizes into a series of alternating along-slope jets with strongly asymmetrical contributions to the slope energy and momentum budgets. Cross-shore variations in the potential vorticity gradient cause the jets to drift continuously offshore, suggesting that fronts observed in regions of AABW down-slope flow may in fact be transient features.

1. Introduction

The Antarctic Slope Front (ASF) encircles almost the entire Antarctic continent and modulates exchanges of waters between the open ocean and the continental shelf (Jacobs 1991). Shoreward Ekman transport, forced by the prevailing easterly winds, can drive warm summer surface waters beneath East Antarctic ice shelves (Zhou et al. 2014) but largely act to keep the Antarctic continental shelf waters cold and fresh (Spence et al. 2014). Intrusions of warm circumpolar deep water (CDW) from middepth offshore have the potential to accelerate melting of Antarctica's marine-terminating glaciers in the coming decades (Hellmer et al. 2012; Favier et al. 2014), as has already been reported in the Amundsen Sea (Rignot and Jacobs 2002; Jacobs et al. 2011). Formation of Antarctic Bottom Water (AABW) ventilates the abyssal ocean (Orsi et al. 2001; Gordon 2009) and takes up heat and CO_2 from the atmosphere (Skinner et al. 2010; Purkey and Johnson 2013). The export of AABW is sensitive to the surface buoyancy fluxes around the Antarctic continent (Stewart et al. 2014; Newsom et al. 2016) and may control the arrangement of the global overturning circulation over millennial time scales (Ferrari et al. 2014; Burke et al. 2015).

In the present work, we focus on sections of the ASF that admit AABW export, such as the Weddell and Ross Seas (Muench and Gordon 1995; Gordon 2009) and parts of East Antarctica (Ohshima et al. 2013), in which we expect all of the physical processes outlined in the previous paragraph to be simultaneously active. We illustrate the configuration of interest in Fig. 1; Fig. 1a sketches the pathway of the Antarctic Slope Current (ASC), collocated with the ASF, and a pathway via which AABW is ostensibly exported (Nicholls et al. 2009) along

Corresponding author e-mail: Andrew L. Stewart, astewart@atmos.ucla.edu

DOI: 10.1175/JPO-D-16-0145.1

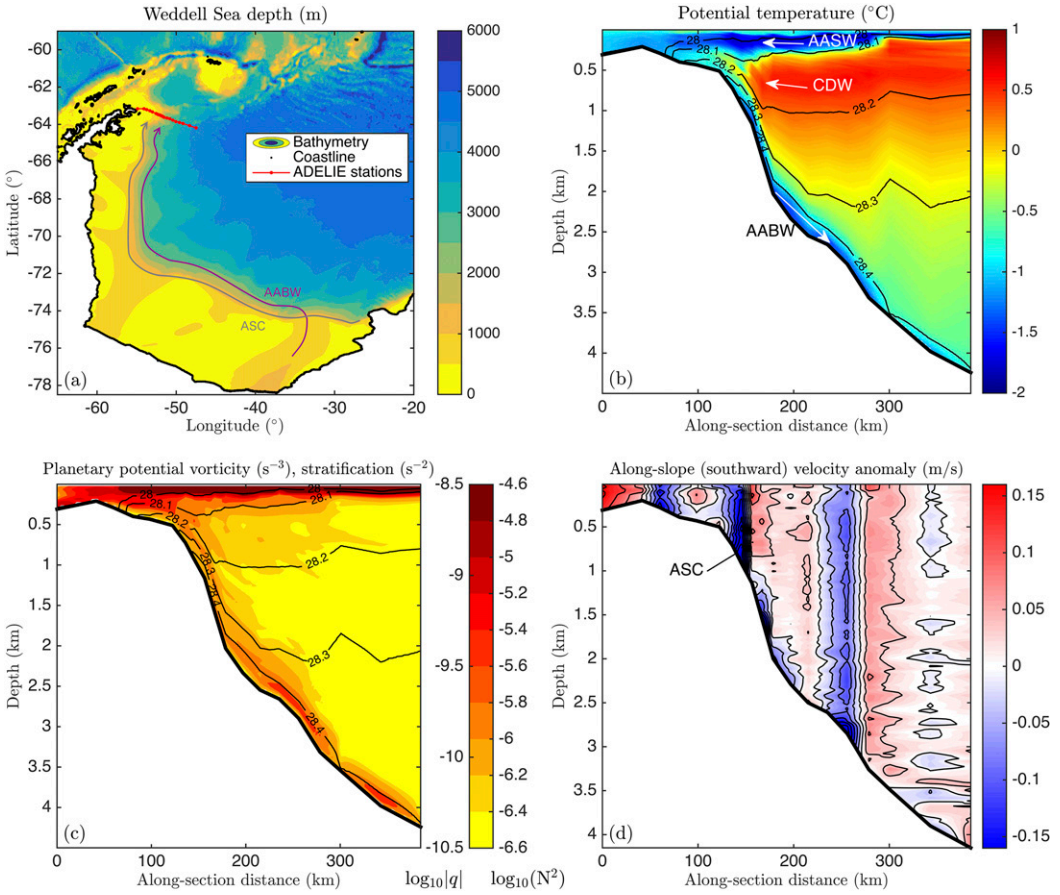

FIG. 1. Overview of the Weddell Sea and water mass transport over the southern/western Weddell Sea continental slope. (a) Bathymetry and coastline of the Weddell Sea, showing the locations of the Antarctic Drifter Experiment: Links to Isobaths and Ecosystems (ADELIE) hydrographic casts (Thompson and Heywood 2008). The arrows indicate the qualitative pathways of the ASC and outflowing AABW. (b) Potential temperature (colors) and neutral density (black contours) from the ADELIE hydrographic casts. Qualitative cross-slope water mass pathways are indicated for AASW, CDW, and AABW. (c) Vertical stratification N^2 and absolute planetary potential vorticity $q = |f|N^2$, contoured in color on a logarithmic scale. (d) Along-slope velocity anomalies (relative to the section-mean along-slope velocity) from lowered acoustic Doppler current profiler (LADCP) data (Thompson and Heywood 2008).

the Antarctic continental slope in the Weddell Sea. Figure 1b shows the major water masses present around the Antarctic margins, taken from hydrographic measurements by Thompson and Heywood (2008), and indicates the directions in which they are transported across the continental slope. We refer to these as Antarctic Surface Water (AASW), CDW, and AABW rather than their Weddell Sea–specific counterparts. Though the modeled water mass properties may only be quantitatively accurate relative to the Weddell Sea, we anticipate that our findings will generalize to other AABW-forming stretches of the Antarctic coastline like the western Ross Sea (see Stewart and Thompson 2015a).

Various recent studies have highlighted the role of mesoscale eddies in facilitating cross-slope exchange around Antarctica. For example, Nøst et al. (2011) and Hattermann et al. (2014a) have shown that mesoscale eddies facilitate intrusions of CDW beneath the Fimbul ice shelf and St-Laurent et al. (2013) have shown that resolving mesoscale eddy motions is necessary to accurately simulate CDW inflow through coastal troughs in West Antarctica. Thompson et al. (2014) and Stewart and Thompson (2015a) found that the ''eddy'' component of the overturning circulation similarly plays a substantial role in transporting CDW onto the continental shelf in the western Weddell Sea. Stewart and Thompson (2012, 2013) and Nakayama et al. (2014) showed that accurate modeling of mesoscale eddies is necessary to represent the descent of AABW down the continental slope.

Despite this mounting evidence supporting the role of mesoscale eddies in the cross-ASF exchange, as yet there has been limited exploration of their generation

mechanisms and dynamical balances. This is at least in part due to the very fine [$O(1)$ km] model grid spacing required to resolve these eddies (St-Laurent et al. 2013; Stewart and Thompson 2015a); there are related logistical difficulties associated with observing their short spatial and temporal scales in the ice-covered Antarctic seas. Here, we explore the genesis of and cross-slope transfer by ASF eddies from a momentum and energy balance perspective. Our aim is to achieve a dynamical understanding with predictive power to guide future observational campaigns and coarse model representations of these eddies.

We are particularly motivated by the possibility that AABW production itself enhances shoreward CDW transport: the downslope flow of AABW necessarily creates an isopycnal connection between the CDW at mid-depth offshore and the waters on the continental shelf. This connection is visible in Fig. 1b and is illustrated by Nicholls et al. (2009). In principle, such a connection facilitates shoreward CDW transport by allowing water parcels to cross the continental slope without doing any work against buoyancy forces. However, the constriction of the isopycnal surfaces creates a strong planetary potential vorticity (PV) gradient due to the shoreward increase of the stratification (see also Thompson et al. 2014), which must be overcome to admit cross-slope CDW transport. This strong PV gradient appears to be accompanied by the formation of multiple along-slope jets, also visible in glider observations (Thompson et al. 2014) and in hydrographic surveys of the eastern Weddell Sea (Chavanne et al. 2010).

In the following sections, we explore these interrelated features of the ASF using an eddy-resolving process model. The structure of this paper is as follows: In section 2, we describe the model configuration. In section 3, we diagnose the role of eddies in exchanging mass and tracers across the continental slope and analyze the momentum and energy budgets to determine how this cross-slope transfer is achieved. In section 4, we show that the mesoscale turbulence over the slope organizes into a series of drifting, alternating, along-slope jets with asymmetric contributions to the momentum and energy budgets. In section 5, we pose a mixing length theory to explain the dependence of the cross-slope exchange on model parameters and test it against a suite of simulations. Finally, in section 6, we discuss our results and provide concluding remarks.

2. Model configuration

In this section, we describe our idealized process model, expanding somewhat upon previous descriptions provided by Stewart and Thompson (2015a,b). The model configuration is summarized schematically in Fig. 2a. Reference values for scalar model parameters discussed below are provided in Table 1.

The design of our model is strongly constrained by the requirements that mesoscale eddies be resolved throughout the domain, that the model be run over a range of forcing and geometrical configurations, and that the model be run long enough to obtain robust eddy statistics. These constraints motivate the use of idealized model forcing and geometry that can be systematically varied and unambiguously analyzed. However, anticipating that nonlinearities in the equation of state may exert significant dynamical influence in this region, it is also desirable to include a realistic representation of the thermohaline stratification. The configuration illustrated in Fig. 2 therefore combines idealized forcing and geometry with realistic stratification, which carries the additional benefit of allowing diagnostics to be posed in terms of a stably stratified neutral density (Jackett and McDougall 1997). Stewart and Thompson (2015a) showed that this model qualitatively reproduces the pycnocline depth and stratification for various parts of the Antarctic margins under suitable variations of the surface wind forcing, though the extent of this comparison is limited because the model always produces AABW.

As shown in Fig. 2b, our model geometry consists of a zonally uniform reentrant Cartesian channel with a shallow continental shelf at the southern boundary.[1] The ocean deepens across a continental slope in the center of the channel to a maximum of 3000 m at the northern boundary. This offshore depth is artificially shallow and has been selected for computational efficiency. More precisely, the ocean depth $h_b(y)$ varies as

$$h_b(y) = \frac{H + H_s}{2} - \frac{H - H_s}{(1 + 4\gamma_s)^{-1/2}} \times \left\{ \left[\frac{1}{4} \sqrt{(1 - Y_s)^2 + 4\gamma_s Y_s^2} - \frac{1}{4} \sqrt{(1 + Y_s)^2 + 4\gamma_s Y_s^2} \right] \right\}, \quad (1)$$

where y is the offshore coordinate and $\gamma_s = 0.05$. We chose reference values of H_s and Y_s that qualitatively reproduce the shape of the continental slope shape in the western Weddell Sea (Amante and Eakins 2009). The model is posed on an f plane, that is, the Coriolis parameter is constant because the Antarctic continental slope is often not zonally oriented and because the topographic vorticity gradient is much larger than the planetary vorticity gradient β in this small domain.

[1] Throughout this paper we use alongshore/zonal and offshore/meridional interchangeably, though our model configuration is more general and need not be aligned longitudinally/latitudinally.

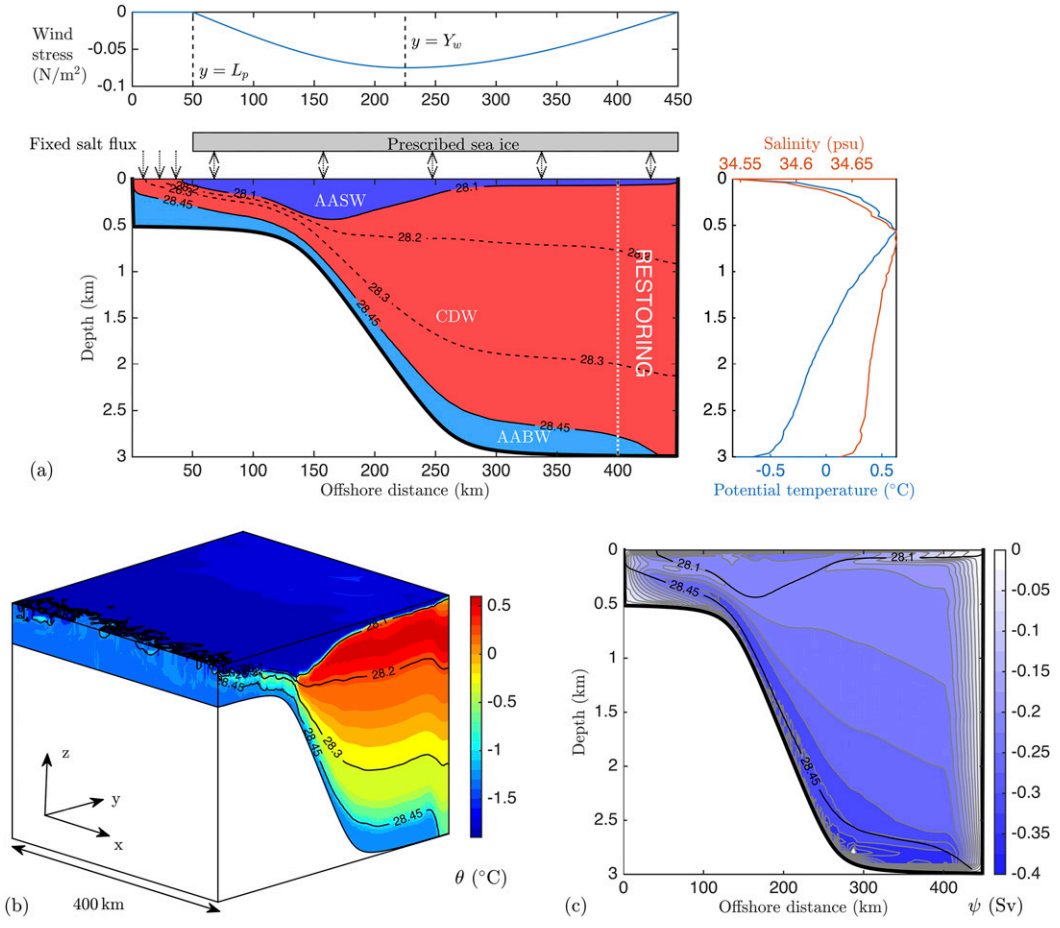

FIG. 2. Summary of our model configuration. (a) Model geometry and forcing. The main panel indicates the division of the time- and alongshore-mean model state into AASW, CDW, and AABW classes along neutral density surfaces. The right-hand panel shows the profiles of potential temperature and salinity toward which the model state is restored at the northern boundary. (b) Snapshot of the potential temperature (colors) and neutral density (black contours) in our reference simulation. (c) Residual overturning streamfunction (colors and gray contours) and time- and alongshore-mean neutral density in our reference simulation; negative values correspond to a counterclockwise circulation.

We integrate the Boussinesq momentum and tracer conservation equations using the MITgcm (Marshall et al. 1997b,a) using the nonlinear equation of state of McDougall et al. (2003). The domain is discretized on a regular horizontal grid with 1-km spacing and a 53-level vertical grid whose spacing ranges from 13 m at the surface to 100 m at the ocean bed. Partial cells are used to improve the resolution of topography, with a minimum wet-cell fraction of 0.1. The model is converged at this grid resolution in the sense that further refinement of the horizontal grid yields no increase in cross-slope transport (Stewart and Thompson 2015a). Potential temperature and salinity are advected using the scheme of Prather (1986), which has been shown to minimize spurious numerical mixing in this model (Hill et al. 2012). Each simulation described herein was initialized with stationary flow and horizontally uniform hydrography from the western Weddell Sea (Thompson and Heywood 2008), modified as described below for the northern sponge region. Each simulation is integrated in time at 2-km horizontal resolution until it achieves a statistically steady state, as determined from the eddy kinetic energy, then interpolated to a 1-km grid and integrated again until it reaches statistically steady at this resolution.

In the southernmost portion of the continental shelf, $y < L_p$, the ocean surface is forced thermodynamically by a fixed surface input of salt per unit area Σ. This crudely parameterizes the input of brine rejection in Antarctic coastal polynyas (Tamura et al. 2008). The remainder of the ocean surface exchanges heat and salt with a parameterized layer of sea ice following the two-equation formulation of Schmidt et al. (2004). More precisely, at every time step surface heat and salt fluxes are calculated based on whether melting or freezing is occurring at the ice shelf base, using the ocean temperature and salinity in the surface grid boxes and the

TABLE 1. List of parameters used in our reference simulation. Italics indicate parameters that are independently varied to test our mixing length theory in section 5.

Parameter	Value	Description
L_x	400 km	Zonal domain size
L_y	450 km	Meridional domain size
H	3000 m	Maximum ocean depth
H_s	500 m	*Continental shelf depth*
Y_s	200 km	Slope center position
W_s	75 km	*Slope half-width*
L_p	50 km	Width of shelf polynya
Σ	2.5 mg m^{-2} s^{-1}	*Polynya salt forcing*
Y_w	225 km	*Peak wind stress position*
L_r	50 km	Width of northern relaxation region
T_r	8 weeks	Northern relaxation time scale
$\tau_{\max}$	0.075 N m^{-2}	*Wind stress maximum*
ρ_0	999.8 kg m^{-3}	Reference density
g	9.81 m^2 s^{-1}	Gravitational constant
f_0	-1.31×10^{-4} s^{-1}	Reference Coriolis parameter f
A_h	12 m^2 s^{-1}	Horizontal viscosity
A_v	3×10^{-4} m^2 s^{-1}	Vertical viscosity
$A_{4\text{grid}}$	0.1	Grid-dependent biharmonic viscosity
$C_{4\text{leith}}$	1.0	Leith vortical viscosity
$C_{4\text{leithD}}$	1.0	Leith solenoidal viscosity
κ_v	5×10^{-6} m^2 s^{-1}	Vertical diffusivity
r_b	1×10^{-3} m s^{-1}	Bottom friction
Δ_x, Δ_y	1 km	Horizontal grid spacing
Δ_z	13–100 m	Vertical grid spacing
Δ_t	179 s	Time step size

TABLE 2. List of parameters used to simulate sea ice forcing at the ocean surface.

Parameter	Value	Description
L_0	3.34×10^5 J kg^{-1}	Latent heat of melting
C_i	2060 J kg^{-1} °C^{-1}	Ice heat capacity
C_p	3994 J kg^{-1} °C^{-1}	Ocean heat capacity
ρ_i	920 kg m^{-3}	Ice reference density
κ_i	1.14×10^{-6} m^2 s^{-1}	Ice thermal diffusivity
γ_T	6×10^{-5} m s^{-1}	Thermal turbulent exchange velocity
H_i	1 m	Ice thickness
ϕ_{fr}	0.14	Salinity retention fraction on freezing
μ	0.054 °C psu^{-1}	Linear saline freezing temperature coefficient
T_i	−5°C	Ice temperature
S_i	5 psu	Ice salinity

prescribed sea ice parameters given in Table 2. However, the calculated melting and freezing rates only serve to change the surface ocean state and not the sea ice state. This sea ice representation does not influence the mechanical forcing of the ocean surface, which is provided by a fixed surface stress as described below. Rather, it is included only to provide thermodynamic forcing of the surface ocean that is representative of the Antarctic margins and which serves to produce a surface layer of AASW with realistic properties.

We impose model stratification at the northern boundary via a sponge layer of width $L_r = 50$ km, in which the potential temperature and salinity fields are restored with a time scale of $T_r = 8$ weeks. We constructed the restoring profiles by interpolating offshore hydrographic data collected by Thompson and Heywood (2008) onto the model's vertical grid. To avoid creating AASW and AABW at the northern boundary, we linearly interpolated the interior (CDW) stratification between depths of 250 and 500 m into the top 250 m of the water column and chose a cast sufficiently far offshore such that there was no signature of AABW above 3000-m depth. The resulting profiles are shown in Fig. 2a.

We force the model mechanically using steady zonally uniform westward surface stress $\tau^{(x)}$, given as

$$\tau^{(x)} = \begin{cases} 0, & y \le L_p, \\ -\tau_{\max} \cos\left(\dfrac{\pi}{2} \dfrac{y - Y_w}{Y_w - L_p}\right), & L_p \le y \le Y_w, \\ -\tau_{\max} \cos\left(\dfrac{\pi}{2} \dfrac{y - Y_w}{L_p - Y_w}\right), & Y_w < y < L_y. \end{cases} \tag{2}$$

Note that the wind stress satisfies $\tau^{(x)} \le 0$ everywhere, corresponding to westward, or prograde, winds. We chose this somewhat convoluted form for (2) because it allows us to vary the amplitude and position of the wind stress maximum, $\tau_{\max}$ and Y_w, respectively, without creating discontinuities in the wind stress or in the wind stress curl. We plot the wind stress profile corresponding to our reference values of $\tau_{\max}$ and Y_w in Fig. 2a. We also impose a linear friction at the ocean bed, with drag coefficient $r_b = 10^{-3}$ m s^{-1} and use biharmonic viscosity to extract energy and enstrophy at the grid scale (see Table 1).

In Fig. 2b, we plot an instantaneous snapshot of the model's three-dimensional potential temperature and neutral density fields. The AASW (cold water at the surface) and CDW (warmer water at middepth) visibly intrude onto the continental shelf, while at the ocean bed AABW descends the continental slope and reaches the northern boundary of the domain. In our reference simulation, we identify the approximate boundaries between these water masses with the 28.1 and 28.45 kg m^{-3} neutral density surfaces, as illustrated in Fig. 2a.

3. Role of eddies in cross-slope exchange

In this section, we quantify the contribution of mesoscale eddies to cross-ASF transfer of mass, heat, and salt

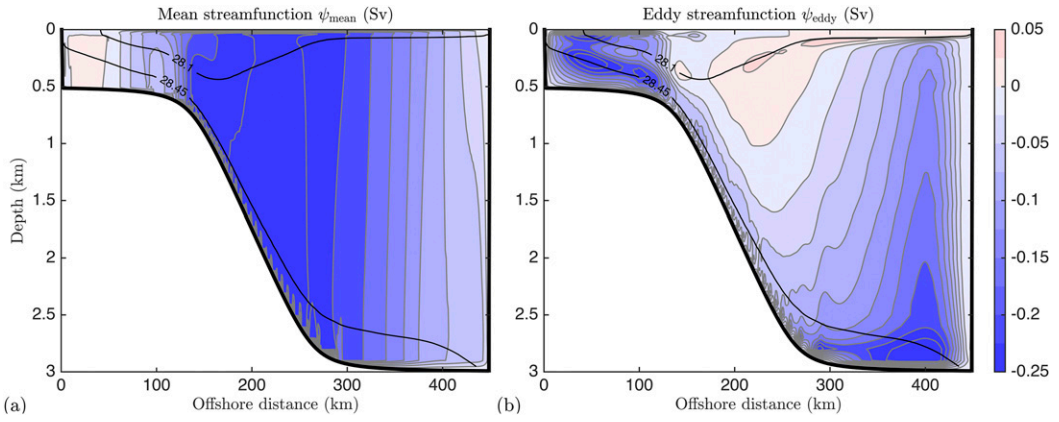

FIG. 3. (a) Mean and (b) eddy components of the residual overturning streamfunction shown in Fig. 2. This decomposition is explained in section 3a. Note that we have converted the streamfunctions into net overturning transports (Sv).

and analyze the energy and momentum budgets to illustrate how this eddy transport is accomplished.

a. Cross-slope mass and tracer fluxes

In Fig. 2c, we quantify the circulation of these water masses using the neutral density transformed Eulerian mean (NDTEM) overturning streamfunction ψ (Stewart and Thompson 2015b), defined as

$$\psi = \psi_{\text{mean}} + \psi_{\text{eddy}}, \tag{3a}$$

$$\psi_{\text{mean}} = \int_z^0 \overline{v}\,\mathrm{d}z, \quad \text{and} \tag{3b}$$

$$\psi_{\text{eddy}} = \frac{\beta(\overline{S},\overline{\theta},z)\overline{v'S'} - \alpha(\overline{S},\overline{\theta},z)\overline{v'\theta'}}{\beta(\overline{S},\overline{\theta},z)\overline{S}_z - \alpha(\overline{S},\overline{\theta},z)\overline{\theta}_z}. \tag{3c}$$

Here, v is the meridional velocity, θ is the potential temperature, S is the salinity, β is the saline contraction coefficient, and α is the thermal expansion coefficient. The overbar $\overline{(\ )}$ denotes a zonal and time average over 5 yr in a statistically steady state, and primes $'$ denote departures of state variables from their respective means.[2] The streamfunction $\psi(y, z)$ quantifies the total northward mass transport above depth z at each latitudinal position y. It approximates the northward mass flux above the isopycnal whose mean depth is equal to z, hence the breakdown into the mean northward flow above z (ψ_{mean}) and an eddy component associated with fluctuations of the isopycnal surface height and velocity (ψ_{eddy}). The NDTEM has been shown to closely approximate the mass fluxes within neutral density surfaces for this model configuration (Stewart and Thompson 2015b).

The streamlines in Fig. 2c support the conceptual overturning indicated in Fig. 1b, with AASW and CDW flowing onto the continental shelf and returning as down-slope flow of AABW. Note that the relatively small cross-slope mass exchange ($\sim$0.3 Sv; 1 Sv $= 10^6\,\mathrm{m^3\,s^{-1}}$) is due to the short zonal domain length. In Fig. 3, we decompose ψ into its mean and eddy components to illustrate the contribution of eddies to the cross-slope exchange. The mean meridional transport is confined to the surface and bottom boundary layers, which admit wind- and frictionally driven ageostrophic flows. Therefore, all of the interior transport of CDW across the slope, and a portion of the AABW return flow, are supplied by eddies. Note, however, that in general the eddy streamfunction ψ_{eddy} is much smaller in magnitude over the continental slope than it is on the continental shelf or in the open ocean. Furthermore, over most of this domain the mean and eddy streamfunctions have the same sign and therefore reinforce one another. Thus, the concept of a "residual" circulation, in which mean and eddy components exactly oppose each other to leading order (e.g., Marshall and Speer 2012) does not hold in this shelf–slope system. This is consistent with previous studies that point to suppression of baroclinic instability over steeply sloping topography (e.g., Pennel et al. 2012; Isachsen 2011; Stewart and Thompson 2013).

Both θ and S vary substantially along the isopycnals crossing the continental slope (see Figs. 1b and 2b), so we can extract additional information about cross-slope eddy transport by considering separately the thermal and saline components of the eddy buoyancy flux. As θ and S

[2] In this section and in section 5, we calculate eddy fluxes exactly, that is, using averages of products over every model time step. In sections 3 and 4, we use instantaneous daily snapshots to calculate all mean and eddy quantities.

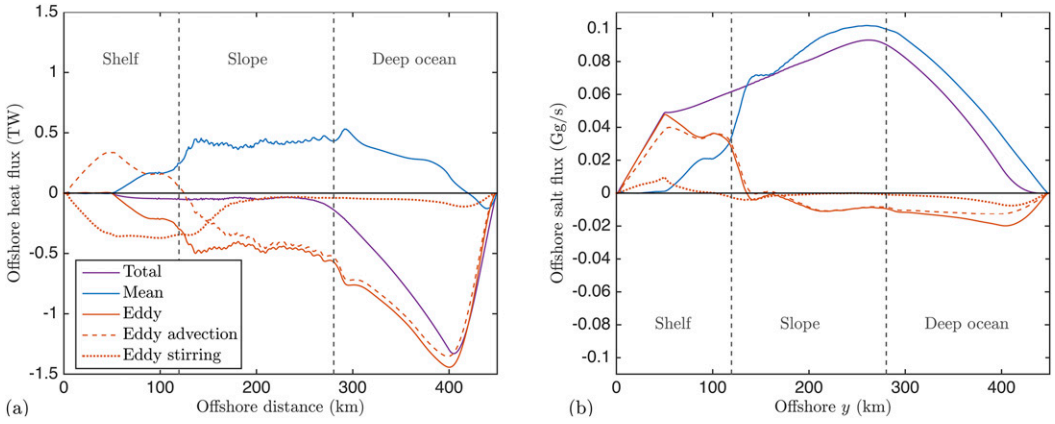

FIG. 4. Offshore fluxes of (a) heat and (b) salt (gigagrams per second), decomposed into mean and eddy components. The eddy component is further decomposed into components due to eddy advection and eddy stirring. The net surface heat and salt fluxes due to thermodynamic exchanges between the ocean and the parameterized sea ice can be inferred from the meridional convergence/divergence of the total fluxes in these plots.

are approximately materially conserved tracers, they may be either advected across the slope by the eddy overturning circulation or simply stirred down their mean gradients along isopycnal surfaces (e.g., Vallis 2006). In Fig. 4, we plot the net meridional fluxes of heat and salt, decomposed into mean and eddy components as

$$F^{(\phi)} = F^{(\phi)}_{\text{mean}} + F^{(\phi)}_{\text{eddy}}, \tag{4a}$$

$$F^{(\phi)}_{\text{mean}} = L_x \int_{-h}^{0} \overline{v}\,\overline{\phi}\,\mathrm{d}z, \quad \text{and} \tag{4b}$$

$$F^{(\phi)}_{\text{eddy}} = L_x \int_{-h}^{0} \overline{v'\phi'}\,\mathrm{d}z, \tag{4c}$$

where $\phi = \theta$ and $\phi = S$, respectively. The variations of $F^{(\theta)}$and $F^{(S)}$ with latitude indicate that sea ice melt is taking place north of $y \approx 270$ km, acting to cool and freshen the ocean. To the south of this, freezing serves to input salt with essentially no impact on the ocean's heat content, and consequently there is approximately no net meridional heat flux. The overall northward salt transport is necessitated by the imposed salt input in the coastal polynya on the continental shelf.

The decomposition of these fluxes into mean and eddy components reveals a contrast between the effects of eddies on the heat and salt budgets. The overall northward salt flux is dominated by the mean flow, due to southward surface Ekman transport of very fresh AASW ($S_{\text{AASW}} \sim 34.3$ psu) and down-slope return flow of much saltier AABW ($S_{\text{AABW}} \sim 34.6$ psu), visible in Fig. 3a. Similarly, the mean component of the heat flux is directed northward because AASW is colder than AABW (~ -1.9°C and ~ -1.5°C, respectively). Over the continental shelf and slope this is almost completely compensated by the southward eddy heat flux, which Fig. 3b suggests is due to shoreward CDW transport. To verify this we further decompose the eddy heat and salt fluxes into components due to eddy advection and eddy stirring:

$$F^{(\phi)}_{\text{eddy}} = F^{(\phi)}_{\text{adv}} + F^{(\phi)}_{\text{stir}}, \quad \text{and} \tag{5a}$$

$$F^{(\phi)}_{\text{adv}} = L_x \int_{-h}^{0} v_{\text{eddy}}\overline{\phi}\,\mathrm{d}z, \tag{5b}$$

where $v_{\text{eddy}} = -\partial\psi_{\text{eddy}}/\partial z$ and $F^{(\phi)}_{\text{stir}}$ is calculated via the residual of $F^{(\phi)}_{\text{eddy}} - F^{(\phi)}_{\text{adv}}$. Conceptually, $F^{(\phi)}_{\text{adv}}$ quantifies cross-slope tracer transports associated with the net volume fluxes of water masses across the slope, and $F^{(\phi)}_{\text{stir}}$ quantifies additional tracer transport due to eddy mixing of heat along isopycnals, which need not be associated with any net volume flux. Figure 4 shows that while eddy advection moves heat southward across most of the domain, at the top of the continental slope there is a "hand over" to eddy stirring, and around the same latitude eddies take over the northward salt flux. This indicates that heat behaves more like a passive tracer on the continental shelf, with salinity dominating the buoyancy gradients.

b. *Properties of shelf/slope eddies*

In Fig. 5b, we plot the eddy kinetic energy (EKE), defined with respect to a time and zonal average (see section 3d). This highlights a puzzling feature of these eddies: the EKE exhibits a local maximum over the continental slope within the CDW layer, despite various previous studies indicating that baroclinic instability is suppressed over steep topography (e.g., Pennel et al. 2012; Isachsen 2011; Stewart and Thompson 2013). Indeed, the EKE in the CDW layer exceeds that found anywhere else in the model domain, including the open

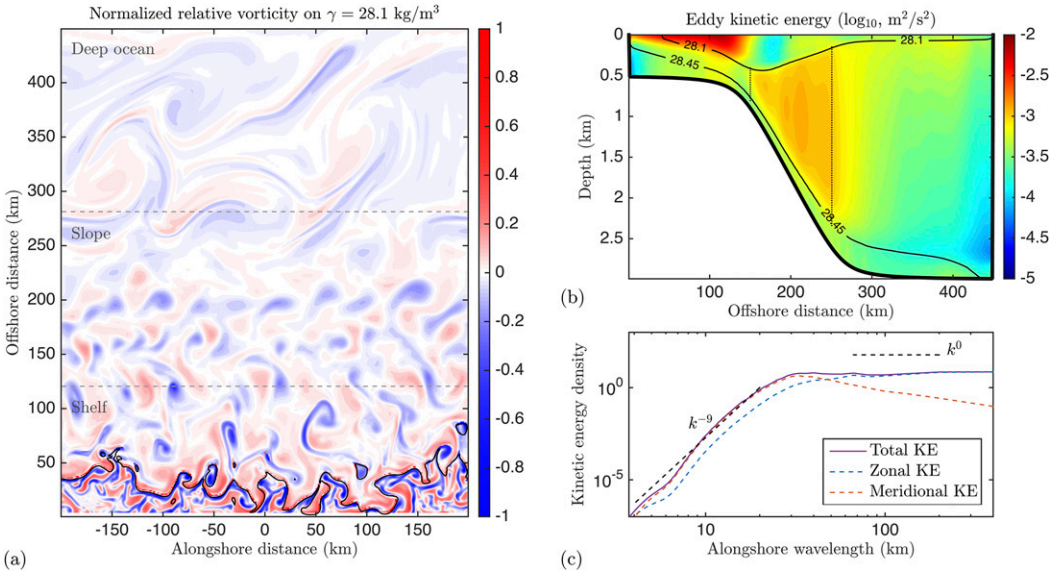

FIG. 5. (a) Normalized relative vorticity ($\mathrm{Ro}_\gamma = \zeta_\gamma/|f_0|$) perpendicular to the neutral density surface $\gamma = 28.1\,\mathrm{kg\,m^{-3}}$. The black curve indicates the position at which this isopycnal outcrops at the ocean surface; within the outcrop region the normalized vertical component of the vorticity ($\mathrm{Ro}_z = \zeta_z/|f_0|$) is plotted instead. (b) Time- and alongshore-mean eddy kinetic energy (colors) and neutral density surfaces (black contours). (c) Alongshore kinetic energy spectrum averaged across the CDW neutral density range over the continental slope [$150 < y < 250$ km, indicated by the dotted lines in (b)].

ocean, with the exception of the top few hundred meters of the water column over the continental shelf. In the following subsections, we will reconcile these properties of the continental slope eddies via analysis of the eddy energy source to the CDW layer and the momentum fluxes that drive southward CDW transport.

Figure 5a provides some insight into these differing turbulent regimes via the normalized relative vorticity (or vortex Rossby number) Ro_γ along the neutral density surface $\gamma = 28.1\,\mathrm{kg\,m^{-3}}$. Here, we define $\mathrm{Ro}_\gamma = \zeta_\gamma/|f_0|$, where $\zeta_\gamma = \partial v/\partial x|_\gamma - \partial u/\partial y|_\gamma$ is the relative vorticity perpendicular to the neutral density surface. In the open ocean the flow is dominated by large-scale [$O(100)$ km] mesoscale eddies with typical Rossby numbers of $|\mathrm{Ro}_\gamma| < 0.1$. Over the continental slope the characteristic length scale of the flow is much smaller [$O(30)$ km], with Rossby numbers around $|\mathrm{Ro}_\gamma| = 0.2$–0.3. On the continental shelf the flow is distinctly submesoscale, featuring $O(10)$ km fronts and filaments and Rossby numbers that regularly reach $|\mathrm{Ro}_\gamma| = 1$–2. These submesoscale features account for the very high EKE over the continental shelf and result from the strong surface buoyancy loss due to salt forcing in the southern portion of the continental shelf (cf. Munday and Zhai 2013).

In Fig. 5c, we focus on the turbulent regime in the CDW layer over the continental slope, plotting its time-/depth-/meridionally averaged kinetic energy (KE) spectrum as a function of zonal wavelength (see, e.g., Vallis 2006, his chapter 8). The total kinetic energy is approximately independent of zonal wavenumber above a wavelength of ~60 km and declines sharply ($\sim k^{-9}$, where k is the wavenumber) for wavelengths smaller than ~30 km. This suggests that grid-scale energy dissipation in the CDW layer over the continental slope is dynamically insignificant. Decomposing the KE into zonal and meridional components reveals that the meridional component dominates at smaller scales and peaks at a wavelength of $\lambda \approx 57$ km, while the zonal component dominates at the largest scales. This suggests a meridional growth of small-scale unstable waves that develop into eddies with a limiting scale of 25–30 km, consistent with Fig. 5a, and a mean along-slope flow at larger scales (see section 4). Note that there is a hint of a $\sim k^{-3}$ spectral slope for wavelengths in the range $30 \lesssim \lambda \lesssim 60$ km, but this is in fact an artifact due to our meridional average across the continental slope. At $y = 150$ km, meridional KE peaks at $\lambda \approx 30$ km, while at $y = 250$ km the meridional KE peaks at $\lambda \approx 60$ km (not shown). The peak at $\lambda \approx 57$ km in Fig. 5c is due to the greater thickness of the CDW layer farther offshore, which gives this part of the continental slope more weight in the depth/meridional average.

c. *Alongshore flow and momentum transfer*

We have thus far established that CDW is transported across the continental slope by an energetic field of small

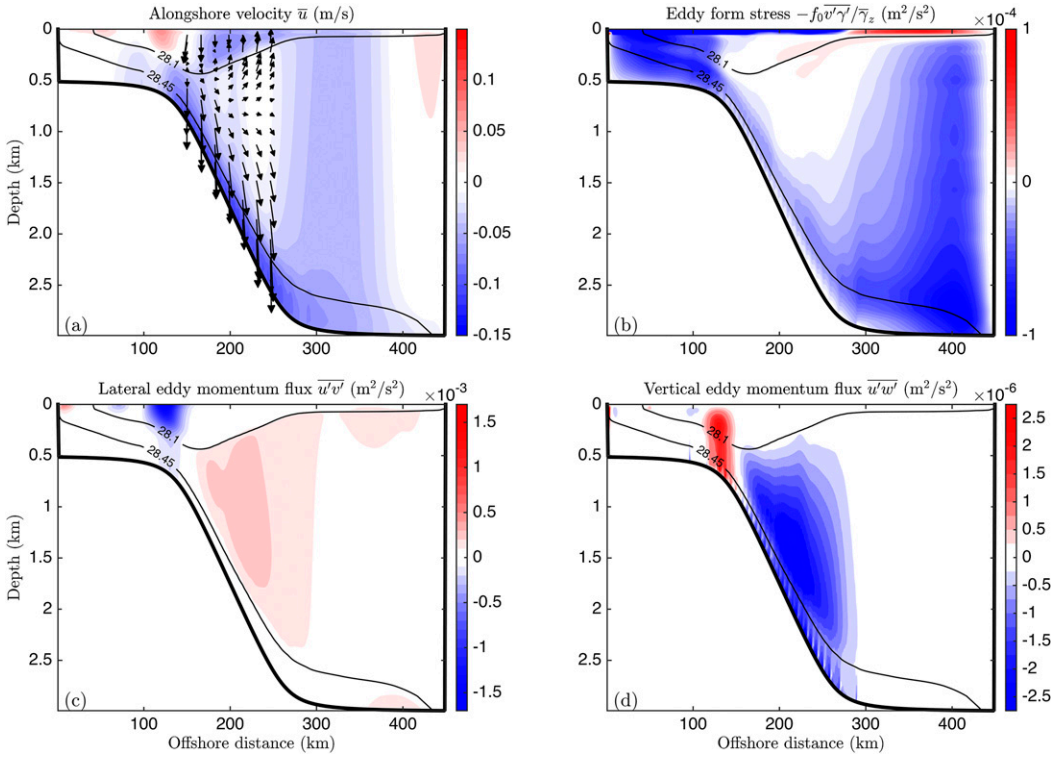

FIG. 6. (a) Time- and alongshore-mean of the alongshore flow and (b)–(d) eddy momentum transfer. (b) The eddy form stress, that is, the vertical eddy diapycnal flux of eastward momentum [see (6)]. The wind stress provides a source of westward momentum at the ocean surface. (c),(d) The Eulerian offshore and vertical eddy momentum fluxes, respectively. The arrows in (a) indicate the direction of the net eddy momentum flux vector. Note the difference in the color scale limits between (b) and (d), emphasizing the dominance of the eddy form stress in the vertical transfer of momentum. This vertical momentum transfer dominates the overall vector flux of momentum, as indicated by the near-vertical arrows in (a).

eddies (~30 km diameter). We now explore how these eddies mechanically drive a southward flow along isopycnals by considering the TEM along-slope momentum balance (e.g., Plumb and Ferrari 2005):

$$\frac{\partial \overline{u}}{\partial t} + \frac{\partial}{\partial y}(\overline{u'v'}) + \frac{\partial}{\partial z}\left(\overline{u'w'} - f_0\frac{\overline{v'\gamma'}}{\overline{\gamma}_z}\right) \approx f\boldsymbol{v}^{\dagger}. \qquad (6)$$

Here, we have retained the time derivative for clarity, though under our 5-yr average this term vanishes approximately. We have also neglected the divergence of the mean momentum flux $\partial_y(\overline{u}\,\overline{v}) + \partial_z(\overline{u}\,\overline{w})$ because it is negligible outside of very narrow surface and bottom boundary layers. Equation (6) therefore states that any southward residual flow $\boldsymbol{v}^{\dagger}$ exerts a Coriolis force that must be balanced by an eddy-induced divergence of eastward momentum or equivalently a convergence of westward momentum. The last term on the left-hand side of (6) approximates the eddy "form stress"—the transfer of momentum between isopycnal layers via horizontal pressure gradients produced by transient eddies (e.g., Vallis 2006).

In Fig. 6, we plot the mean along-slope velocity and the components of the eddy momentum flux vector. Figure 6a shows that the westward along-slope flow is intensified in the AASW and AABW layers but suppressed in the CDW layer, consistent with thermal wind shear across the northward-shoaled pycnocline and southward-shoaled CDW–AABW interface. The westward along-slope flow is opposed by an eastward shelfbreak jet that results from the thermal wind shear imposed by buoyancy loss on the continental shelf; a similar feature can be seen in the observationally derived velocity anomalies in Fig. 1b. The arrows in this panel correspond to the direction and magnitude of the eddy momentum flux vector. They indicate a relatively small flux of eastward momentum upward from the CDW into the AASW layer and a much larger downward flux of eastward momentum from the CDW into the AABW layer. Thus, westward momentum is supplied to the CDW layer from both above and below, producing the convergence of westward momentum that is required to force the shoreward residual flow of CDW along isopycnals. Figures 6b–d show that

these fluxes are dominated by eddy form stress, suggesting that baroclinic instabilities facilitate the vertical momentum transport (this will be verified in section 3d). While the vertical eddy momentum flux $\overline{u'w'}$ is everywhere negligible compared to the eddy form stress, there is a nonnegligible contribution from the northward eddy flux of eastward momentum $\overline{u'v'}$ throughout the CDW layer on the continental slope. The source of this meridional momentum flux will be explored in section 4.

d. Eddy energy budget

Our analysis of the along-slope momentum budget in section 3c suggests that the shoreward CDW transport is mechanically driven by baroclinic instabilities at the pycnocline and at the CDW–AABW interface, providing meridional eddy buoyancy fluxes and thus vertical momentum transfer via form stress. To verify this mechanism and link it to the model's surface forcing, we now consider the EKE budget:

$$\frac{\partial}{\partial t}\mathrm{EKE} + \nabla\cdot\mathbf{F}_{\mathrm{EKE}} = (\mathrm{MKE}\rightarrow\mathrm{EKE}) + (\mathrm{PE}\rightarrow\mathrm{EKE}). \tag{7}$$

Here, we have again retained the time derivative of the EKE for clarity, though it should approximately vanish under our 5-yr time average. The Boussinesq MKE and EKE per unit mass are defined respectively as

$$\mathrm{MKE} = \frac{1}{2}\overline{\mathbf{u}}_h^2, \tag{8}$$

and

$$\mathrm{EKE} = \frac{1}{2}\overline{\mathbf{u}_h'^2}, \tag{9}$$

where $\mathbf{u}_h = (u, v)$ denotes the horizontal velocity vector. The meridional/vertical vector EKE flux is defined as

$$\mathbf{F}_{\mathrm{EKE}} = \frac{1}{2}\overline{\mathbf{u}_h'^2(\overline{\mathbf{u}}+\mathbf{u}')} + \overline{\mathbf{u}'\phi'}, \tag{10}$$

where $\phi = p/\rho_0$ is the dynamic pressure divided by the reference density. The right-hand side of (7) consists of conversion terms between energy reservoirs:

$$(\mathrm{MKE}\rightarrow\mathrm{EKE}) = -\overline{\mathbf{u}_h'\cdot(\mathbf{u}'\cdot\nabla)\overline{\mathbf{u}}_h}, \quad \text{and} \tag{11a}$$

$$(\mathrm{PE}\rightarrow\mathrm{EKE}) = \overline{w'b'}, \tag{11b}$$

which denote the conversion of mean kinetic energy (MKE) to EKE and of potential energy (PE) to EKE, respectively. Here, $b = -g(\rho - \rho_0)/\rho_0$ denotes the buoyancy. To simplify the presentation of (7), we have neglected external sources and sinks of energy, specifically those due to bottom drag and explicit/numerical viscosity.

The steady surface wind forcing can only provide a source of MKE, rather than EKE, in our model configuration. However, this energy input may ultimately be converted to EKE via the PE. We therefore also consider the energy conversion from MKE to PE, which we define as

$$(\mathrm{MKE}\rightarrow\mathrm{PE}) = \psi_{\mathrm{mean}}\frac{\partial b}{\partial y} = -\overline{w}\,\overline{b} - \nabla\cdot(\psi_{\mathrm{mean}}b\hat{\mathbf{y}}). \tag{12}$$

This equation differs from the intuitive definition $(\mathrm{MKE}\rightarrow\mathrm{PE}) = -\overline{w}\,\overline{b}$ by the divergence of a meridional flux, as indicated by the rightmost equality in (12). Thus, in the domain average these definitions are identical, but locally our definition is more informative (see Fig. 7).

In Figs. 7a–c, we plot the conversions of energy between PE, EKE, and MKE. The dominant source of EKE over the slope is baroclinic conversion [(PE → EKE)], as suggested by the dominant vertical momentum transfer by eddy form stress in Fig. 6. This occurs principally at the CDW–AABW interface, rather than the pycnocline, despite the stronger density stratification across the pycnocline. Figure 7b shows that the conversion between MKE and EKE is dynamically significant only at the shelf break, where it accomplishes a net southward transport of EKE via conversion to MKE in the eastward shelfbreak jet (see Fig. 6) and subsequent release back to EKE farther south. Figure 7c shows that the principal role of the wind is actually to remove potential energy by reducing the tilt of isopycnals, which are generally shoaled to the south (cf. the mean overturning circulation and deep isopycnal tilt in Fig. 3a). This PE is sourced from the salt input at the ocean surface on the continental shelf, which simultaneously energizes the submesoscale eddies on the shelf and provides a source of PE to the continental slope via advection of AABW. The wind-induced removal of PE from the stratification is larger by a factor of 3 than the conversion of PE to EKE at the CDW–AABW interface. This indicates that the westward surface winds largely suppress deep eddy generation over the continental slope and that the primary route to dissipation for shelf-sourced PE is actually via conversion to MKE and then extraction by bottom drag.

A key feature of the energy conversion terms is that they are all negligible in the CDW layer over the continental slope, yet this region exhibits locally elevated EKE (see Fig. 5b). In Fig. 7d, we examine the fluxes of EKE to determine how the CDW layer is energized. The arrows indicate the direction and magnitude of the EKE flux vector $\mathbf{F}_{\mathrm{EKE}}$. This plot reveals that the CDW layer is energized by a convergence of vertical energy fluxes

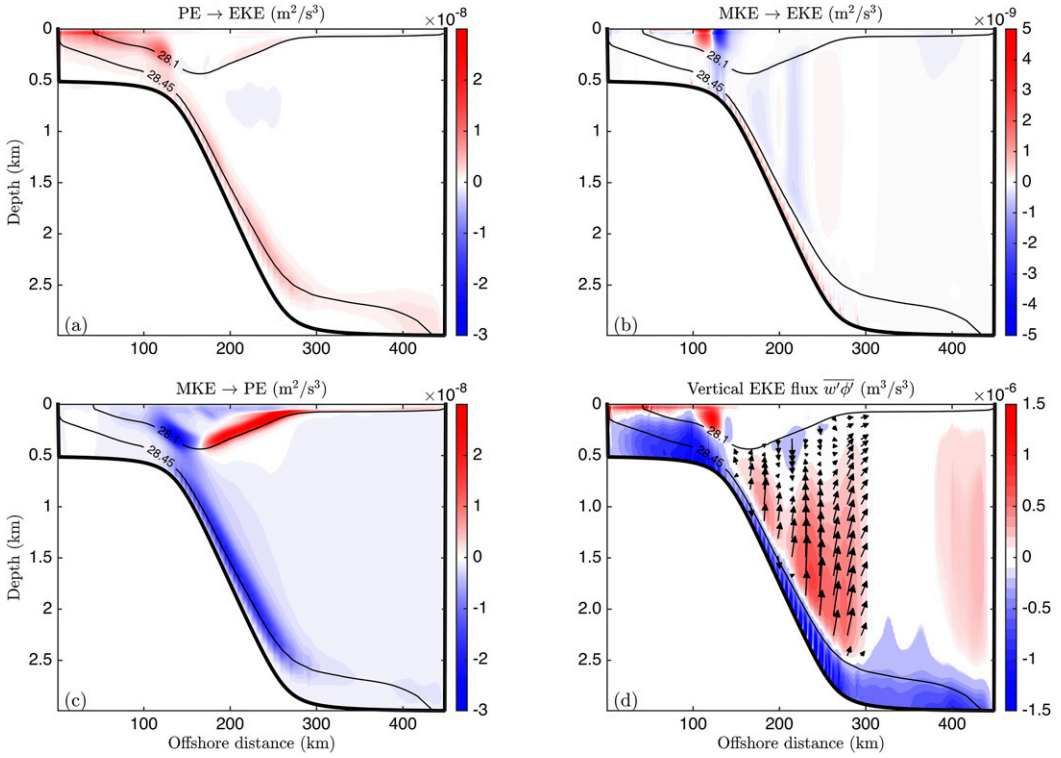

FIG. 7. Sources of EKE supplying the eddies over the continental slope. (a) Baroclinic conversion from PE to MKE. (b) Barotropic conversion from MKE to EKE. (c) Conversion from MKE to PE due to tilting and untilting of isopycnals by the mean vertical velocity (see Fig. 3). (d) EKE fluxes. Black arrows indicate the direction of the net EKE flux within the CDW density classes over the continental slope. The net flux is dominated everywhere by the quasigeostrophic vertical EKE flux $\overline{w'\phi'}$, plotted in color.

from the pycnocline and the CDW–AABW interface, though mainly from the latter. The flux vector is dominated by the quasigeostrophic vertical EKE flux $\overline{w'\phi'}$, contours of which are also plotted in Fig. 7d. This is consistent with our analysis of the momentum budget in section 3c; baroclinic instability taking place at the CDW–AABW interface, and to a lesser extent at the pycnocline, releases PE into EKE and produces a convergence of energy and westward momentum into the CDW layer. This provides the mechanical forcing and energizes the mesoscale eddies required to drive CDW onto the continental shelf.

4. Dynamics of along-slope jets

Our analysis of the momentum and energy budgets in section 3 explains how eddy energy is supplied to the CDW layer and how CDW is forced mechanically onto the continental shelf along isopycnals. However, given that dissipation is negligible because kinetic energy is essentially absent at the smallest resolved scales (see Fig. 5c), it is unclear from Fig. 7 what limits the accumulation of energy in the CDW layer. In this section, we show that this apparent mismatch in the EKE budget over the continental slope is actually the result of aliasing from slowly drifting along-slope jets.

a. Jet circulation and momentum balance

In the presence of a strong topographic potential vorticity gradient, turbulent geostrophic flow may be expected to undergo an inverse cascade of energy until it reaches the "wave turbulence boundary" (Vallis and Maltrud 1993; Rhines 1994). Beyond this point, the growth of energy is preferentially perpendicular to the potential vorticity gradient, that is, favoring the generation of multiple along-slope jets. However, while some structure is apparent in the mean along-slope velocity in Fig. 6a, there is no clear signature of multiple jets.

Figure 8 shows that there are in fact multiple along-slope jets that drift continuously across the continental slope. The jets' velocities are small (a few centimeters per second) relative to the westward velocities in the AASW and AABW layers but typically exceed the mean westward velocity in the CDW layer, so both westward and eastward jets are typically found over the slope in any given model snapshot. Figure 8a shows the anomaly in

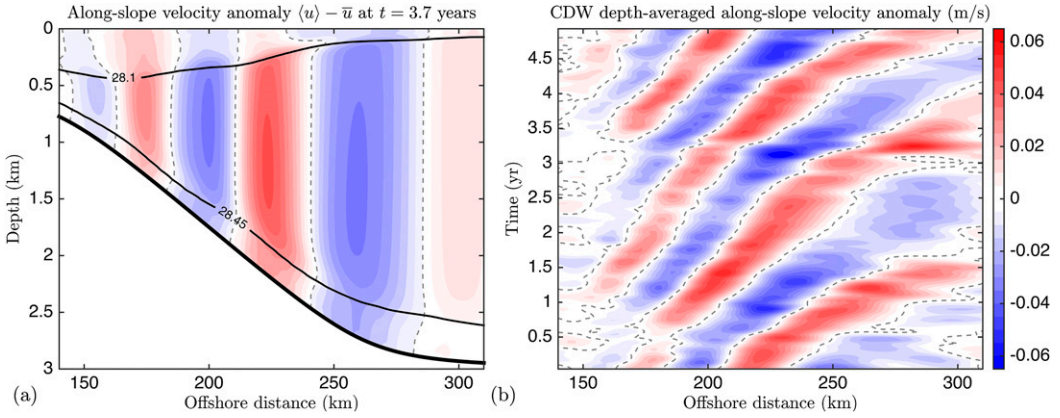

FIG. 8. Transient jets over the continental slope. (a) Along-slope velocity anomaly from an average taken over 30 days and along the continental slope $\langle u \rangle$, relative to the 5-yr mean velocity $\overline{u}$. (b) Hovmöller (1949) diagram of the along-slope velocity anomaly, constructed from consecutive running 30-day averages.

the along-slope velocity averaged over a representative 30-day period in the simulation, denoted as $\langle u \rangle$, relative to the 5-yr mean velocity $\overline{u}$. This averaging period was selected because it is short relative to the jet drift rate, but long compared to the eddy turnover time scale over the continental slope, which is on the order of a few days. The jets extend throughout the water column but are intensified in the CDW layer and are associated with a steeper (shallower) isopycnal tilt in the eastward (westward) jets. In Fig. 8b, we plot a Hovmöller (1949) diagram of the along-slope velocity as a function of cross-slope distance and time, constructed using running 30-day averages of the along-slope velocity averaged over the CDW layer. Both eastward and westward jets form close to the shelf break, around $y = 150$ km, and drift steadily offshore. The jet width broadens from around 30 km at the top of the slope to around 50 km at the bottom, with an accompanying acceleration in the drift rate from around 25 km yr^{-1} at the top to around 50 km yr^{-1} at the bottom. The jet width is everywhere much larger than the first Rossby radius of deformation, which is around 4 km over the continental slope.

To examine how these jets modulate the transport of CDW across the continental slope, in Figs. 9 and 10 we return to the momentum and energy budgets discussed in section 3. For the purposes of this section, (6)–(12) should be reinterpreted in terms of averages over a 30-day window (i.e., $\langle\,\rangle$) rather than the 5-yr average $\overline{(\ )}$, with primes $'$ denoting deviations from the 30-day average.

In section 3c, we showed that the lateral eddy momentum flux and vertical eddy form stress are the dominant contributions to the net momentum flux vector (indicated via arrows) over the continental slope. Figures 9a and 9b reveal that these fluxes are in fact strongly tied to the structure of the along-slope jets; the eddy form stress is concentrated in the core of the eastward jets, while the lateral eddy momentum flux is concentrated at the southern flanks of the eastward jets. This differs from the behavior of quasigeostrophic jets, based on which one might expect the lateral momentum fluxes occur at all jet flanks, transferring eastward momentum out of the westward jets and into the eastward jets (Lee 1997).

The asymmetry in the momentum transfer between the eastward and westward jets may be expected to result in asymmetries in the residual circulation, which approximately balances the net momentum flux convergence [cf. (6)]. Figure 9c shows that the lateral eddy momentum fluxes support local anomalies in the mean overturning streamfunction ψ_{mean}, which reinforces the sense of the wind-driven overturning circulation (see Fig. 3) in the westward jets and opposes it in the eastward jets. Figure 9b indicates that the eddy overturning circulation is strongly enhanced in the eastward jets but suppressed in the westward jets (recall that that eddy streamfunction ψ_{eddy} differs from eddy form stress approximately by a factor of $-f_0$).

Despite these interjet variations of the mean and eddy streamfunctions, Fig. 9d shows that residual net shoreward transport in the CDW layer is in fact approximately uniform across the continental slope. However, this analysis reveals that the cross-slope transport is accomplished via distinct mechanisms in the westward and eastward jets. In the center of the continental slope, the mean overturning circulation in the westward jets complements the eddy transport and is of approximately the same magnitude; in the eastward jets, the mean overturning circulation opposes the eddies and compensates around 50% of their shoreward transport.

Finally, we note that in Fig. 9 we have not examined the time evolution of the mean flow $\partial\langle u \rangle/\partial t$, which may be

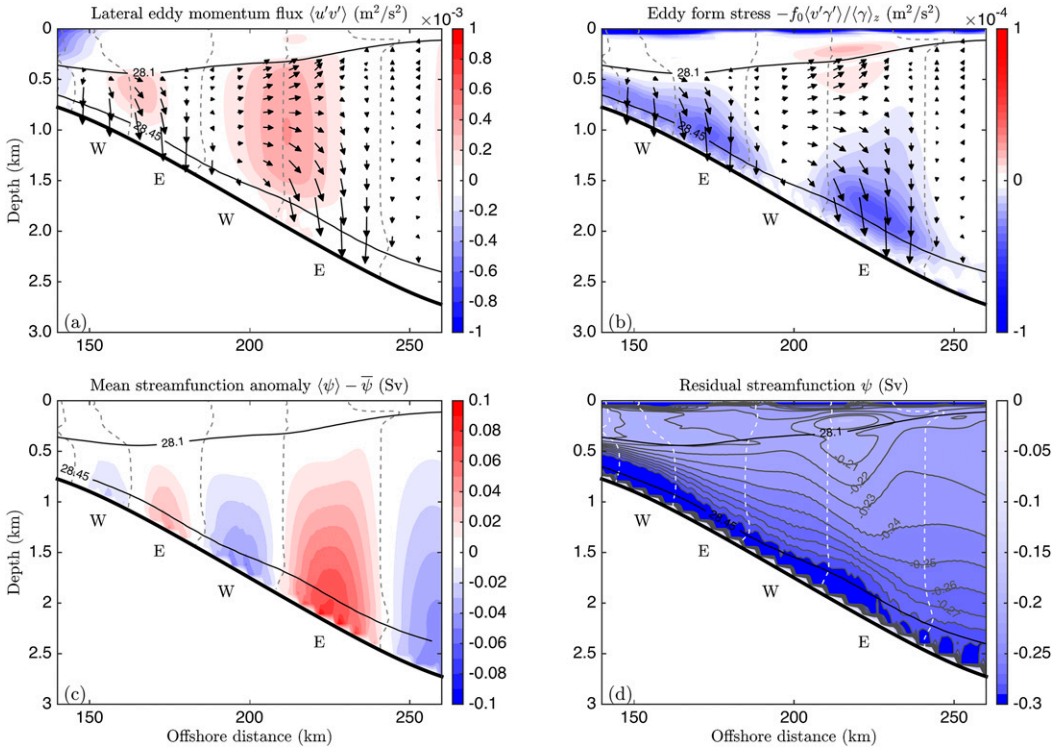

FIG. 9. Momentum balance of continental slope jets at $t = 3.7$ yr [refer to (6)]. In each panel the black contours show the neutral density and the dashed gray contours show the jet boundaries, each averaged over 30 days and along the continental slope. (a) Lateral eddy momentum flux and (b) vertical eddy form stress, with arrows indicating the direction of the full eddy momentum flux vector within the CDW density classes. (c) Anomaly in the mean overturning streamfunction ($\langle \psi \rangle$), relative to the 5-yr mean overturning streamfunction ($\overline{\psi}$). (d) Residual overturning streamfunction.

expected to bear a signature of the jets' down-slope drift. However, this term is typically orders of magnitude smaller than the other terms in (6).

b. *Jet-scale energy budget*

To understand the asymmetry in the momentum fluxes between the eastward and westward jets, we now consider the eddy energy budget at the jet scale. Figure 10a shows that the EKE is concentrated in the eastward jets, with a bias toward the southern jet flanks, consistent with the locations of enhanced eddy momentum fluxes in Fig. 9. As in Fig. 7, the EKE is sourced principally from baroclinic conversion at the CDW–AABW interface close to the ocean bed. However, Fig. 10b shows that this conversion and injection of EKE occurs almost entirely within the eastward jets. Intuitively, this is because the eastward CDW jets oppose the direction of the flow in the AASW and AABW layers and are therefore necessarily associated with stronger vertical shear and thus baroclinicity. Crucially, in the eastward jets the isopycnals are more steeply sloped than the topography; the inset in Fig. 10a shows the topographic parameter, defined as the ratio of the topographic slope to the isopycnal slope (Mechoso 1980) for the $\gamma = 28.45\,\mathrm{kg\,m^{-3}}$ isopycnal. Linear baroclinic instability theory therefore predicts that the eastward jets should be unstable (Mechoso 1980; Isachsen 2011), whereas the westward jets may be expected to be stable.

To characterize the processes responsible for extracting the EKE injected into the CDW layer, we must consider not only the budget for EKE, but also for MKE:

$$\frac{\partial}{\partial t}\mathrm{MKE} + \nabla \cdot \mathbf{F}_{\mathrm{MKE}} + (\mathrm{MKE} \to \mathrm{EKE}) + (\mathrm{MKE} \to \mathrm{PE}) = 0. \tag{13}$$

Here, the meridional/vertical vector MKE flux is defined as

$$\mathbf{F}_{\mathrm{MKE}} = \frac{1}{2}\mathbf{u}\langle \mathbf{u} \rangle_h^2 + \langle \mathbf{u}'(\langle \mathbf{u}_h \rangle \cdot \mathbf{u}_h') \rangle - \psi_{\mathrm{mean}} \frac{\partial \langle \phi \rangle}{\partial y}\hat{\mathbf{z}}, \tag{14}$$

where ψ_{mean}, (MKE → EKE), and (MKE → PE) follow their definitions in (3b), (11a), and (12) but with 5-yr averages $\overline{(\ )}$ replaced by 30-day averages $\langle\ \rangle$. The final

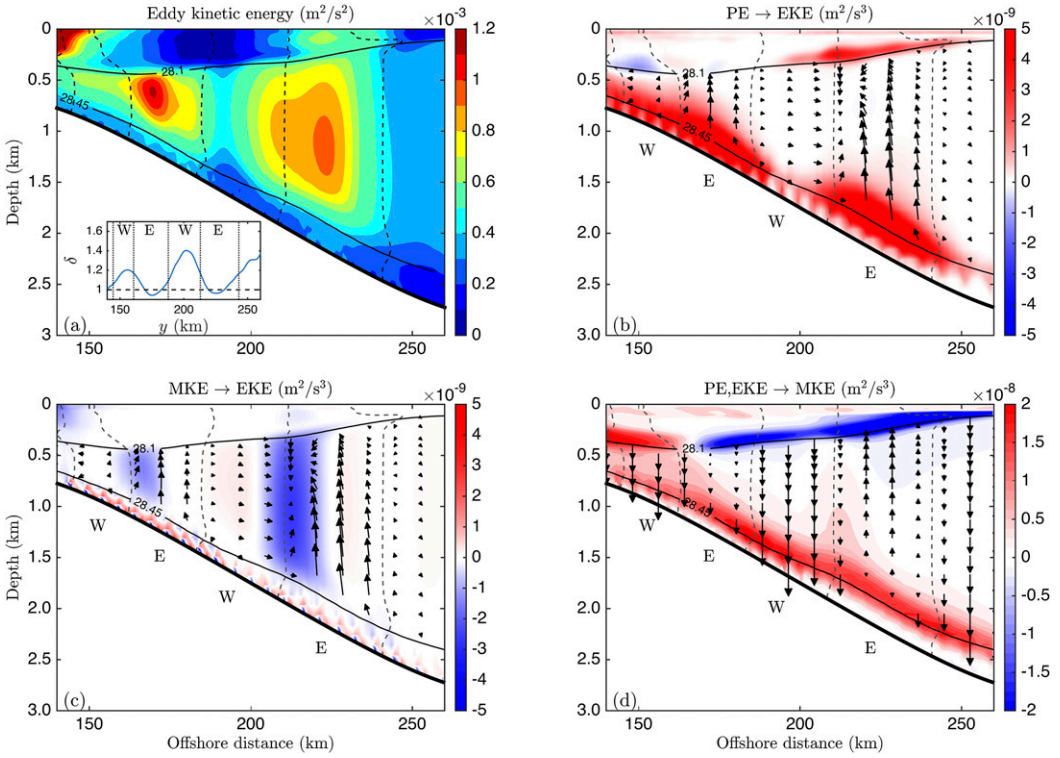

FIG. 10. Energy fluxes and transformations within continental slope jets at $t = 3.7$ yr (cf. with Fig. 8). In each panel the black contours show the neutral density and the dashed gray contours show the jet boundaries, each averaged over 30 days and along the continental slope. The labels W and E indicate whether the jets are directed westward or eastward. (a) EKE. (b) Baroclinic conversion from PE to EKE. (c) Barotropic conversion from MKE to EKE. (d) Combined production of MKE via conversion from PE and EKE. In (b) and (c), the arrows indicate the direction of the net EKE flux vector within the CDW density range. In (d), the arrows indicate the direction of the net MKE flux within the CDW density range. The inset in (a) shows the topographic parameter δ = (topographic slope)/(isopycnal slope) as a function of offshore distance for the $\gamma = 28.45\,\mathrm{kg\,m^{-3}}$ isopycnal. The isopycnal slope was smoothed using a Gaussian kernel regression filter with a width of 3 km in order to remove small-scale noise due to steps in the topographic slope on the model's z-coordinate grid.

term in (14) is the result of a cancellation between the pressure flux term $\langle \mathbf{u} \rangle \langle \phi \rangle$ and the lateral buoyancy flux term on the right-hand side of (12).

In Fig. 10c, we show that EKE is principally extracted from the CDW layer via conversion to MKE at the southern flanks of eastward jets, resulting from strong northward eddy momentum flux from the westward jets to the eastward jets (see Fig. 9). This energy conversion makes a relatively minor contribution to the MKE budget, shown in Fig. 10d, compared to the large conversions to and from PE at the pycnocline and the CDW–AABW interface. However, it provides a necessary route to dissipation for EKE in the CDW layer; after being converted to MKE at the southern flanks for the eastward jets, the energy is transferred downward and removed by bottom friction at the ocean bed. This vertical MKE flux is indicated by arrows in Fig. 10d and is dominated by the vertical pressure flux term in (13).

However, there is a mismatch between the EKE and MKE flux convergences and the conversion from EKE to MKE over the continental slope in Fig. 10. Some mismatch is to be expected because the jets are translating down the continental slope and thus the time derivatives of the EKE and MKE are nonzero. However, as suggested by Fig. 8b, there is also substantial temporal variability in the MKE and EKE of each jet. Though on average the tendencies in the MKE and EKE serve to translate the EKE/MKE structure of the jets down the continental slope, this signal is swamped by the fluctuations in the EKE and MKE within each jet. As a result, none of the monthly averaged snapshots unambiguously exhibit the patterns of MKE/EKE convergence/divergence required to translate the jets down the slope, namely, an enhancement of the MKE at the jet flanks, a suppression of EKE at the southern flanks of the eastward jets, and an enhancement of the EKE at the northern flanks of the eastward jets. This temporal

variability also explains the apparent unbalanced convergence of energy in the CDW layer in Fig. 7; the 5-yr average used to create this figure only spans the passage of ~3 eastward/westward jet pairs, which is insufficient to obtain a completely converged diagnosis of the long-time mean eddy energy fluxes.

5. Mixing length theory for cross-slope eddy transfer

In this section, we attempt to translate the results of our momentum/energy budget analyses in sections 3 and 4 into a predictive theory for the cross-slope transfer of CDW mass and heat energy. The key insight lies in the relation between the cross-slope CDW mass flux, which determines the heat flux in most of the simulations examined here, and the EKE in the CDW layer over the continental slope, which serves as an input parameter for the mixing length theory described below. Though in principle it may also be possible to constrain the EKE based on the model parameters, it is not clear that such a theory would have utility beyond the particular idealized model configuration used in this paper. We therefore leave the more general problem of constraining the EKE in shelf/slope mesoscale turbulence for future work.

The key ingredients of our theory are illustrated schematically in Fig. 11. We conceptually divide the water column at each latitude into three layers of thickness h_i (i = AASW, CDW, AABW), each assumed to have uniform potential temperature θ_i and salinity S_i for simplicity. The overturning circulation consists of shoreward mass fluxes of AASW (F_{AASW}) and CDW (F_{CDW}), which exactly balanced by an offshore transport of AABW (F_{AABW}). This conceptual decomposition of the water masses and overturning circulation is similar to that introduced by Ou (2007). Our discussion below pertains to the fluxes across the center of the continental slope, around $y = 200$ km.

a. Overturning circulation

Motivated by our diagnosis of the overturning circulation in section 3a, we assume that the shoreward transport of AASW is accomplished entirely by wind-driven Ekman transport (see also Zhou et al. 2014; Stewart and Thompson 2013, 2015a),

$$F_{\mathrm{AASW}} = \tau_{\mathrm{max}}/\rho_0|f_0|, \tag{15}$$

and that the shoreward transport of CDW is supported by an eddy thickness flux:

$$F_{\mathrm{CDW}} = \kappa\frac{\partial h_{\mathrm{CDW}}}{\partial y}, \tag{16}$$

where κ is the buoyancy or thickness diffusivity. The offshore transport of AABW balances the total shoreward mass flux:

$$F_{\mathrm{AABW}} = F_{\mathrm{AASW}} + F_{\mathrm{CDW}}. \tag{17}$$

Rather than parameterize the exact gradient of the thickness of the CDW layer ($\partial h_{\mathrm{CDW}}/\partial y$), which is a priori unknown, we simply approximate this term by the gradient of the water column thickness:

$$\frac{\partial h_{\mathrm{CDW}}}{\partial y} \approx s_b = \frac{H - H_s}{2W_s}, \tag{18}$$

where s_b is the maximum absolute topographic slope. Using the actual CDW layer thickness gradient diagnosed from our simulations does not qualitatively change the results.

Equations (15)–(18) constitute a closed theory for the overturning circulation, with the exception of the thickness diffusivity κ. We construct a parameterization for κ using mixing length theory (Taylor 1922), assuming that it is proportional to the product of a characteristic eddy velocity u_{eddy} and a mixing length l_{mix}:

$$\kappa = Cu_{\mathrm{eddy}}l_{\mathrm{mix}}, \tag{19}$$

where C is a constant that will be defined below. In each simulation considered below, we diagnose u_{eddy} as

$$u_{\mathrm{eddy}} = \sqrt{\frac{2}{A_{\mathrm{slope}}}\iint_{\mathrm{slope}} dy\,dz\ \ \mathrm{EKE}}, \tag{20}$$

where $\iint_{\mathrm{slope}}$ denotes an integral over the full water column depth and over the latitude range $-W_s < y - Y_s < W_s$, and A_{slope} denotes the corresponding area in the y–z plane. Motivated by our analysis of the along-slope jets in section 4, we define the mixing length as the topographic Rhines scale:

$$L_{\mathrm{Rh}} = \pi\sqrt{\frac{2u_{\mathrm{eddy}}}{\beta_t}}, \quad \beta_t = \frac{|f_0|}{h_{\mathrm{CDW}}}\left|\frac{\partial h_{\mathrm{CDW}}}{\partial y}\right|, \tag{21}$$

where β_t is the topographic vorticity gradient. Here, we again parameterize $\partial h_{\mathrm{CDW}}/\partial y$ following (18), and we consistently approximate the layer thickness as $h_{\mathrm{CDW}} = 0.5(H + H_s)$. Note that in (21) we have used the barotropic Rhines scale because the along-slope jets in Fig. 8a have a substantial barotropic component, though the baroclinic Rhines scale may also be relevant here (Williams and Kelsall 2015). For our reference simulation, (21) predicts a jet width of 26 km, which is within the range of jet widths diagnosed in section 4.

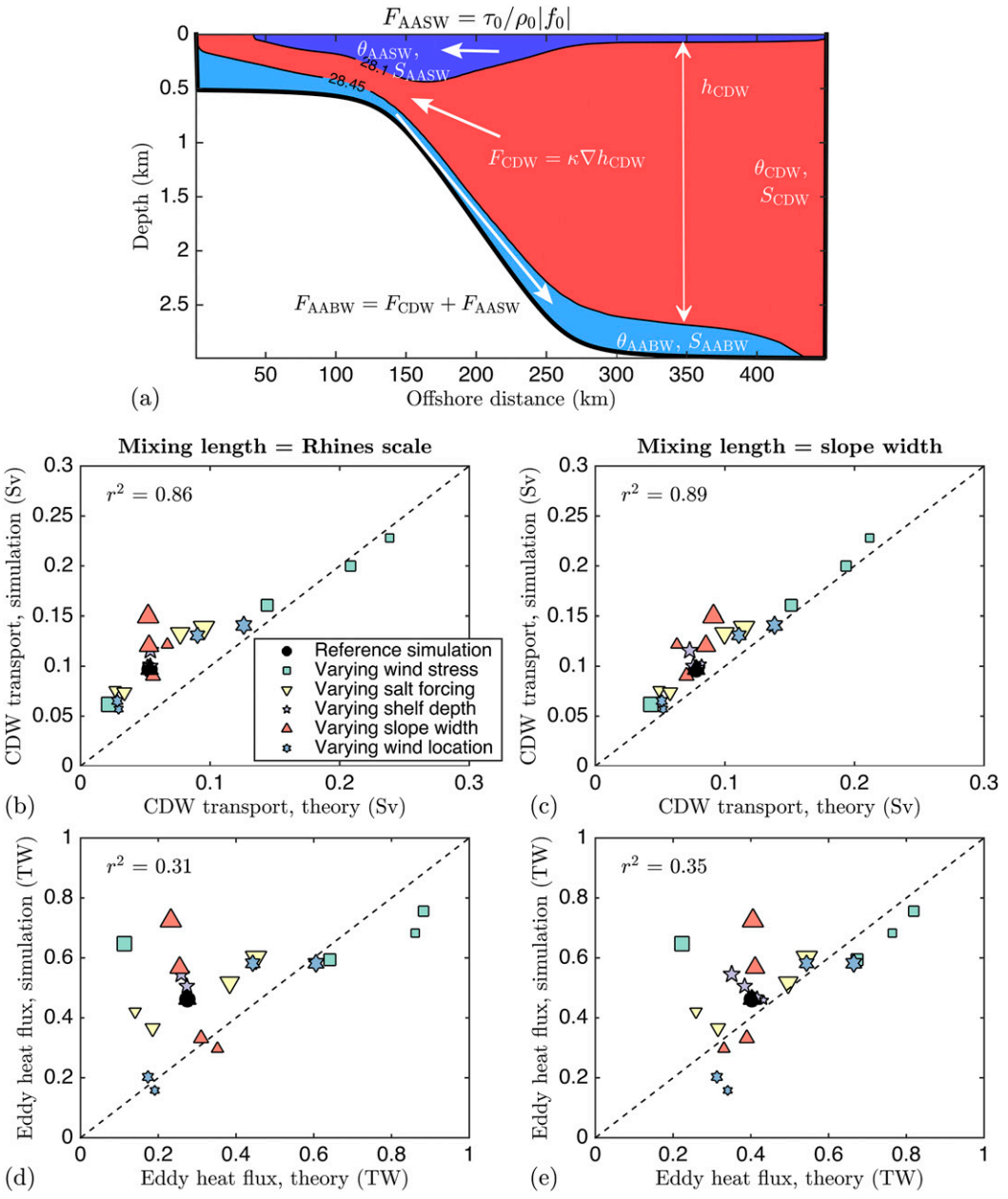

FIG. 11. (a) Summary of our conceptual model of water mass exchange across the Antarctic continental shelf and slope. Comparison between our conceptual model prediction for (b),(c) the midslope shoreward CDW transport and (d),(e) the shoreward eddy heat flux. In (b) and (d), we have set the mixing length equal to the topographic Rhines scale (Rhines 1975), while in (c) and (e) we have set the mixing length equal to the slope width. Different marker colors/shapes correspond to the different variations in the simulation setup reported by Stewart and Thompson (2015a), with increasing marker sizes corresponding to increasing values of the various parameters. The correlation coefficients quoted in each panel are all statistically significant at the 1% level.

To complete our parameterization of κ, we must assign a constant of proportionality in (19). Visbeck et al. (1997) found that a constant value of $C = 0.015$ accurately parameterized the buoyancy diffusivity across a range of numerical model simulations of different baroclinically unstable flows, so we anticipate that this value might similarly apply to the ASF. However, our analysis of the jet-scale momentum budget in section 4a showed that in the eastward jets, where the EKE is concentrated, around 50% of the shoreward eddy transport is compensated by an offshore jet-scale mean flow. We therefore prepend a factor of ½ to the constant C in (19), yielding

$$\kappa_{\mathrm{Rh}} = \frac{1}{2} C_{\mathrm{Rh}} u_{\mathrm{eddy}} L_{\mathrm{Rh}}, \tag{22}$$

where $C_{\mathrm{Rh}} = C_{\mathrm{V97}} = 0.015$ is the Visbeck et al. (1997) eddy transfer coefficient.

An alternative and arguably simpler basis for prescribing the mixing length, but one that neglects the nuances of along-slope jet formation, is simply to set l_{mix} equal to the slope width, under the assumption that this sets the "width of the baroclinic zone" (Visbeck et al. 1997). This yields an alternative parameterization of the thickness diffusivity:

$$\kappa_s = C_s u_{\mathrm{eddy}} (2W_s). \tag{23}$$

In this case, we use $C_s = (1/8) C_{\mathrm{V97}}$ because it offers a good fit to our model results, but this choice has no basis in established theory.

In Figs. 11b–c, we compare the cross-slope CDW transport F_{CDW} predicted by this theory against that diagnosed by calculating the overturning streamfunction (3a) in a range of simulations with varying model parameters (see Stewart and Thompson 2015a). Both parameterizations, κ_{Rh} and κ_s, yield similarly strong correlations ($r^2 \approx 0.9$) between the theoretical, diagnosed, cross-slope transports of CDW. However, κ_s produces a better absolute match between the theory and simulations with a root-mean-square error of 0.027 Sv, compared to 0.046 Sv when κ_{Rh} is used. The key difference between κ_{Rh} and κ_s lies in the way that the diffusivity scales with the EKE and topographic slope. When the mixing length is set equal to the Rhines scale, they are related via

$$\kappa_{\mathrm{Rh}} \propto (\mathrm{EKE})^{3/4} s_b^{-1/2}, \tag{24}$$

whereas when the mixing length is set equal to the slope width,

$$\kappa_s \propto (\mathrm{EKE})^{1/2} s_b^{-1}, \tag{25}$$

where we have used $2W_s = (H - H_s)/s_b$ and assumed that $H - H_s$ remains approximately constant between experiments. For example, κ_{Rh} is unable to reproduce the changes in CDW transport across our experiments with varying continental slope width, in which s_b changes by a factor of 5, whereas κ_s fairs somewhat better. Note that (25) results in a net shoreward CDW transport that scales only with EKE, that is, $F_{\mathrm{CDW}} \propto (\mathrm{EKE})^{1/2} s_b^0$, a result that does not have a clear interpretation based on our analyses of the momentum and energy budgets in sections 3–4.

b. Heat transport

As a further test of the predictive power of our mixing length–based theory, we draw on our finding in Fig. 4a that the shoreward heat flux over the continental slope is principally due to eddy advection, rather than eddy stirring. Assuming that advection accounts for the entire cross-slope heat flux, the net cross-slope heat flux $F^{(\theta)}$ may be derived from (4a) as

$$F^{(\theta)} = F_{\mathrm{AABW}} \theta_{\mathrm{AABW}} - F_{\mathrm{CDW}} \theta_{\mathrm{CDW}} - F_{\mathrm{AASW}} \theta_{\mathrm{AASW}}. \tag{26}$$

Here, we assume that the potential temperature of the CDW layer is set by offshore processes and equal to $\theta_{\mathrm{CDW}} = 0°\mathrm{C}$. We further assume that the AASW over the continental slope is at the freezing temperature, taken to be $\theta_{\mathrm{AASW}} = -1.85°\mathrm{C}$, due to its thermodynamic interaction with the overlying sea ice. In principle the potential temperature of the AABW layer θ_{AABW} may be determined by balancing the cross-slope heat transport [(26)] against the heat loss at the surface over the continental shelf. However, the surface heat flux depends on the interaction of the ocean with the overlying sea ice and is difficult to estimate a priori, so instead we diagnose θ_{AABW} as the time- and zonal-mean potential temperature at the ocean bed in the center of the continental slope ($y = 200\,\mathrm{km}$).

Finally, recall that the heat flux associated with shoreward transport of AASW is due to the wind-driven mean shoreward Ekman transport, while the heat flux associated with shoreward transport of CDW is due to eddy transport (Figs. 3, 4). We therefore assume that the full, cross-slope heat flux [(26)] may be decomposed into mean and eddy components (defined positive offshore) as

$$F^{(\theta)}_{\mathrm{mean}} = -F_{\mathrm{AASW}} (\theta_{\mathrm{AASW}} - \theta_{\mathrm{AABW}}), \quad \text{and} \tag{27a}$$

$$F^{(\theta)}_{\mathrm{eddy}} = -F_{\mathrm{CDW}} (\theta_{\mathrm{CDW}} - \theta_{\mathrm{AABW}}). \tag{27b}$$

In Figs. 11d and 11e, we compare the predictions of (27b) against $F^{(\theta)}_{\mathrm{eddy}}$ diagnosed from various model simulations, using the Rhines scale or the slope width as the eddy mixing length in defining F_{CDW}. In these panels the agreement between the theory and the simulations is less satisfactory than for the CDW mass transport in Figs. 11b and 11c. The most notable source of discrepancy lies in the experiments with varying surface wind stress and varying slope width (square and triangular symbols in Figs. 11d and 11e). When the wind stress is reduced, the wind extracts less energy from the deep stratification at the CDW–AABW interface, leading to a greater baroclinic release of potential energy. A broader continental slope produces a similar effect because the shallower topographic slope is less effective at suppressing baroclinic instability. In both cases, the more energetic eddies over the continental slope—almost an order of magnitude larger in the case of zero surface wind

stress than in our reference simulation—more efficiently stir tracers across the continental slope. As a result, our assumption of a purely advective cross-slope heat exchange leads to an underestimate of the eddy heat flux.

6. Discussion and conclusions

The ASF occupies a critical location in the near-Antarctic and global ocean circulation because it supports a range of salient water mass exchanges between the open ocean and the Antarctic continental shelf, many of which are mediated by the genesis of mesoscale eddies (e.g., Zhang et al. 2011; St-Laurent et al. 2013; Zhou et al. 2014; Stewart and Thompson 2015a; Nakayama et al. 2014). In this study, we have used an idealized, eddy-resolving process model to elucidate the dynamics of these eddies along bottom water–forming stretches of the Antarctic coastline.

a. Key results

We partly motivated this work in section 1 by the prospect that AABW outflow might passively facilitate shoreward heat transport by creating an isopycnal connection between the continental shelf waters and the CDW layer offshore. In sections 3a and 3b, we verified this mechanism; in our model, the shoreward transports of heat and mass are supported by eddy thickness fluxes along isopycnals.[3] However, in section 3c we showed that the export of AABW also actively drives shoreward heat transport by converging westward momentum into the CDW layer, as is required to mechanically force CDW across the continental slope. The vertical momentum flux takes the form of an eddy form stress and coincides with release of available potential energy at the CDW–AABW interface. This injects energy into the CDW layer, producing a local maximum in EKE that is ultimately sourced from buoyancy loss on the continental shelf. This bottom-up eddy transfer of momentum and energy stands in contrast with the canonical view of the Antarctic Circumpolar Current (ACC), in which surface winds supply momentum and energy that is subsequently transported downward by eddy fluxes (Tréguier and McWilliams 1990), though more recent studies suggest that a similar, bottom-up supply of momentum and energy may also be at work in the ACC (Ward and Hogg 2011; Howard et al. 2015). The enhancement of EKE in the subsurface CDW layer also poses a challenge to future observational campaigns around the Antarctic margins, as it has a limited surface signature.

In section 4, we showed that the continental slope hosts a series of alternating along-slope jets, qualitatively similar to those found in recent observations (Thompson and Heywood 2008; Thompson et al. 2014). These jets continually drift down the continental slope, vanishing in a sufficiently long time average, suggesting that the fronts in the in situ measurements may in fact be transient features. The jet-scale momentum and energy balances demonstrate that the eddy fluxes of momentum and energy to the CDW layer occur almost entirely in the eastward jets, which oppose the mean flow of the ASF and therefore have greater baroclinicity. We interpreted this asymmetry from the standpoint of linear baroclinic instability theory (Mechoso 1980; Isachsen 2011), which suggests that only the eastward jets should be baroclinically unstable because there the isopycnals dividing the CDW and AABW layers are more steeply sloped than the bottom topography. The eastward jets may also be expected to more rapidly mix tracers along isopycnals because their mean flow opposes the direction of topography Rossby wave/eddy propagation (Ferrari and Nikurashin 2010). The formation of multiple along-slope jets has been reported previously in a conceptually similar model configuration with no surface wind forcing (Spall 2013). The down-slope drift of the jets is consistent with the quasigeostrophic and primitive equation model results of Stern et al. (2015), who showed that jets tend to drift toward regions of lower absolute barotropic potential vorticity gradient because this favors more rapid growth of baroclinic instabilities and therefore supplies more energy to the jets (see also Thompson 2010).

In section 5, we combined previous theory (Visbeck et al. 1997) with key findings from previous sections to propose two mixing length–based parameterization strategies for the eddy thickness diffusivity over the continental slope, treating the slope EKE as a known parameter. Both parameterizations have skill in predicting the cross-slope CDW mass flux and the simulated shoreward eddy heat fluxes, though the assumptions used to predict the latter break down as the surface wind stress weakens. We found the predictive skill of the parameterization based on slope width–constrained mixing to be superior to that of the parameterization based on Rhines scale–constrained mixing, despite the stronger physical motivation for the latter. However, the slope width–based parameterization is more ad hoc in that the constant of proportionality C has been chosen simply to obtain a fit. The Rhines scale–based parameterization has no undetermined constants because it is directly modified from Visbeck et al. (1997), in light of which the agreement

[3] Note that shoreward eddy transport of CDW does not strictly require an isopycnal connection between the CDW layer and the continental shelf (Nøst et al. 2011), but in our model they are closely related (Stewart and Thompson 2015a).

between the theory and simulations in Fig. 11b is remarkably close.

b. Caveats and outlook for further research

As outlined in section 2, we employed an idealized model configuration because it allowed us to resolve eddies across a range of model parameters while preserving realistic near-Antarctic ocean stratification (Stewart and Thompson 2015a). However, this idealization carries various caveats that we regard as avenues for further work. For example, our model does not include a representation of tides, which contribute to AABW production via water mass transport by tidal residual flows and via diapycnal mixing due to breaking internal waves (Padman et al. 2009). Flexas et al. (2015) have shown that tides can generate ASF-like structures at the shelf break, even without surface wind forcing. Our model configuration also cannot accurately represent down-slope gravity currents, by which newly formed dense shelf water spills out onto the continental slope (e.g., Gordon et al. 2004, 2009). Though our model cannot represent the initial gravity-driven flow and resulting entrainment in these currents, it can capture the later stages of their evolution when they adjust to form geostrophic, bottom-trapped, along-isobath flows (Gordon et al. 2015).

While we purposefully minimized the complexity of the surface forcing in our model, in reality AABW formation depends on a series of processes that are not represented here. In particular, we exclude the formation of Ice Shelf Water (ISW), which is the lightest water mass along some stretches of the coastline (e.g., Hattermann et al. 2014b). The interaction of these shelf processes and seasonal surface buoyancy fluxes with mesoscale turbulence over the continental slope remains unexplored. Additionally, the strong seasonal variations in surface buoyancy forcing at these latitudes lead to a pronounced annual cycle in the formation of high-salinity shelf water (HSSW; e.g., Assmann et al. 2003) and in the properties of the surface waters (e.g., Park et al. 1998), both of which may influence the cross-slope heat transport and the formation of along-slope jets. Our representations of the surface wind forcing and ice–ocean thermodynamic exchanges are also highly idealized and neglect the subtleties associated with transmission of stress through sea ice (Uotila et al. 2000). The cyclonic winds that circulate around the Weddell Gyre, for example, also have a pronounced seasonal cycle that modulates the export of AABW (e.g., Wang et al. 2012; Su et al. 2014). We performed a simulation using a simple annual cycle with an amplitude of $0.05\,\mathrm{N\,m^{-1}}$ in the strength of the surface wind stress but found that this did not impact the overall cross-slope transport of CDW. It is also possible that higher-frequency variability in the winds might directly influence the EKE and jet formation in the CDW layer.

A key element to be addressed in future work is the role of alongshore asymmetries in modulating cross-slope eddy transport of CDW. In analogy with ACC (e.g., Abernathey and Cessi 2014; Thompson and Naveira Garabato 2014), topographic features in the path of the current may be expected to focus the heat transport across the ASC. As part of this work we performed several simulations that (i) included a topographic anomaly, for example, trough or ridge, on the shelf and slope, (ii) localized the brine input over the continental shelf, and (iii) shifted the spatial displacement of the brine injection and topographic anomaly. In all cases we found that there was little impact on the eddy transport of CDW across the center of the continental slope. This is consistent with the findings of Spall (2013), who introduced troughs and ridges into a simulation of dense water formation over an island and found that, in along-isobath coordinates, the system behaved identically to a case without troughs and ridges. Importantly, as reported in previous modeling studies and in situ observations (e.g., St-Laurent et al. 2013; Kohut et al. 2013), including a trough in the continental shelf efficiently steers the CDW toward the coast once it has reached the top of the continental slope. However, our exploration of the influence of alongshore topographic variations on cross-slope eddy transport is too preliminary to draw firm conclusions and warrants further study. Further study is also required to determine the applicability of our zonally periodic shelf/slope channel model to AABW formation sites like the southern Weddell Sea, where the overturning circulation is fundamentally three-dimensional (Nicholls et al. 2009). The export of AABW through the Filchner depression lies upstream (in the ASC) of the Ronne polynya, which is responsible for the majority of the HSSW formation on the continental shelf. It is conceivable that the processes described in this paper could apply in a three-dimensional sense, with the rate of AABW export upstream of the Ronne polynya modulating the rate of shoreward CDW transport around the polynya itself.

Acknowledgments. ALS's research was supported by NSF Award OCE-1538702. AFT's research was funded by NSF Award OPP-124646. Some of the simulations presented herein were conducted using the CITerra computing cluster in the Division of Geological and Planetary Sciences at the California Institute of Technology, and the authors thank the CITerra technicians for facilitating this work. The data presented in this article are available from the authors on request. The authors gratefully acknowledge the modeling efforts of the MITgcm team. The authors also thank Tore Hattermann and an anonymous

reviewer for many constructive comments that improved the manuscript.

REFERENCES

Abernathey, R., and P. Cessi, 2014: Topographic enhancement of eddy efficiency in baroclinic equilibration. *J. Phys. Oceanogr.*, **44**, 2107–2126, doi:10.1175/JPO-D-14-0014.1.

Amante, C., and B. W. Eakins, 2009: ETOPO1 1 arc-minute global relief model: Procedures, data sources and analysis. NOAA Tech. Memo. NESDIS NGDC-24, 25 pp. [Available online at https://www.ngdc.noaa.gov/mgg/global/relief/ETOPO1/docs/ETOPO1.pdf.]

Assmann, K., H. H. Hellmer, and A. Beckmann, 2003: Seasonal variation in circulation and water mass distribution on the Ross Sea continental shelf. *Antarct. Sci.*, **15**, 3–11, doi:10.1017/S0954102003001007.

Burke, A., A. L. Stewart, J. F. Adkins, R. Ferrari, M. F. Jansen, and A. F. Thompson, 2015: The glacial mid-depth radiocarbon bulge and its implications for the overturning circulation. *Paleoceanography*, **30**, 1021–1039, doi:10.1002/2015PA002778.

Chavanne, C. P., K. J. Heywood, K. W. Nicholls, and I. Fer, 2010: Observations of the Antarctic slope undercurrent in the southeastern Weddell Sea. *Geophys. Res. Lett.*, **37**, L13601, doi:10.1029/2010GL043603.

Favier, L., and Coauthors, 2014: Retreat of Pine Island Glacier controlled by marine ice-sheet instability. *Nat. Climate Change*, **4**, 117–121, doi:10.1038/nclimate2094.

Ferrari, R., and M. Nikurashin, 2010: Suppression of eddy diffusivity across jets in the Southern Ocean. *J. Phys. Oceanogr.*, **40**, 1501–1519, doi:10.1175/2010JPO4278.1.

——, M. F. Jansen, J. F. Adkins, A. Burke, A. L. Stewart, and A. F. Thompson, 2014: Antarctic sea ice control on ocean circulation in present and glacial climates. *Proc. Natl. Acad. Sci. USA*, **111**, 8753–8758, doi:10.1073/pnas.1323922111.

Flexas, M., M. P. Schodlok, L. Padman, D. Menemenlis, and A. H. Orsi, 2015: Role of tides on the formation of the Antarctic Slope Front at the Weddell-Scotia Confluence. *J. Geophys. Res. Oceans*, **120**, 3658–3680, doi:10.1002/2014JC010372.

Gordon, A. L., 2009: Bottom water formation. *Ocean Currents*, J. H. Steele, S. A. Thorpe, and K. K. Turekian, Eds., Associated Press, 263–269.

——, E. Zambianchi, A. Orsi, M. Visbeck, C. F. Giulivi, T. Whitworth, and G. Spezie, 2004: Energetic plumes over the western Ross Sea continental slope. *Geophys. Res. Lett.*, **31**, L21302, doi:10.1029/2004GL020785.

——, A. H. Orsi, R. Muench, B. A. Huber, E. Zambianchi, and M. Visbeck, 2009: Western Ross Sea continental slope gravity currents. *Deep-Sea Res. II*, **56**, 796–817, doi:10.1016/j.dsr2.2008.10.037.

——, B. A. Huber, and J. Busecke, 2015: Bottom water export from the western Ross Sea, 2007 through 2010. *Geophys. Res. Lett.*, **42**, 5387–5394, doi:10.1002/2015GL064457.

Hattermann, T., L. H. Smedsrud, O. A. Nøst, J. M. Lilly, and B. K. Galton-Fenzi, 2014a: Eddy-resolving simulations of the Fimbul Ice Shelf cavity circulation: Basal melting and exchange with open ocean. *Ocean Modell.*, **82**, 28–44, doi:10.1016/j.ocemod.2014.07.004.

——, ——, ——, ——, and ——, 2014b: Eddy-resolving simulations of the Fimbul Ice Shelf cavity circulation: Basal melting and exchange with open ocean. *Ocean Modell.*, **82**, 28–44, doi:10.1016/j.ocemod.2014.07.004.

Hellmer, H. H., F. Kauker, R. Timmermann, J. Determann, and J. Rae, 2012: Twenty-first-century warming of a large Antarctic ice-shelf cavity by a redirected coastal current. *Nature*, **485**, 225–228, doi:10.1038/nature11064.

Hill, C., D. Ferreira, J.-M. Campin, J. Marshall, R. Abernathey, and N. Barrier, 2012: Controlling spurious diapycnal mixing in eddy-resolving height-coordinate ocean models—Insights from virtual deliberate tracer release experiments. *Ocean Modell.*, **45–46**, 14–26, doi:10.1016/j.ocemod.2011.12.001.

Hovmöller, E., 1949: The trough-and-ridge diagram. *Tellus*, **1A**, 62–66, doi:10.1111/j.2153-3490.1949.tb01260.x.

Howard, E., A. M. Hogg, S. Waterman, and D. P. Marshall, 2015: The injection of zonal momentum by buoyancy forcing in a Southern Ocean model. *J. Phys. Oceanogr.*, **45**, 259–271, doi:10.1175/JPO-D-14-0098.1.

Isachsen, P. E., 2011: Baroclinic instability and eddy tracer transport across sloping bottom topography: How well does a modified Eady model do in primitive equation simulations? *Ocean Modell.*, **39**, 183–199, doi:10.1016/j.ocemod.2010.09.007.

Jackett, D. R., and T. J. McDougall, 1997: A neutral density variable for the world's oceans. *J. Phys. Oceanogr.*, **27**, 237–263, doi:10.1175/1520-0485(1997)027<0237:ANDVFT>2.0.CO;2.

Jacobs, S. S., 1991: On the nature and significance of the Antarctic Slope Front. *Mar. Chem.*, **35**, 9–24, doi:10.1016/S0304-4203(09)90005-6.

——, A. Jenkins, C. F. Giulivi, and P. Dutrieux, 2011: Stronger ocean circulation and increased melting under Pine Island Glacier ice shelf. *Nat. Geosci.*, **4**, 519–523, doi:10.1038/ngeo1188.

Kohut, J., E. Hunter, and B. Huber, 2013: Small-scale variability of the cross-shelf flow over the outer shelf of the Ross Sea. *J. Geophys. Res. Oceans*, **118**, 1863–1876, doi:10.1002/jgrc.20090.

Lee, S., 1997: Maintenance of multiple jets in a baroclinic flow. *J. Atmos. Sci.*, **54**, 1726–1738, doi:10.1175/1520-0469(1997)054<1726:MOMJIA>2.0.CO;2.

Marshall, J., and K. Speer, 2012: Closure of the meridional overturning circulation through Southern Ocean upwelling. *Nat. Geosci.*, **5**, 171–180, doi:10.1038/ngeo1391.

——, A. Adcroft, C. Hill, L. Perelman, and C. Heisey, 1997a: A finite-volume, incompressible Navier Stokes model for studies of the ocean on parallel computers. *J. Geophys. Res.*, **102**, 5753–5766, doi:10.1029/96JC02775.

——, C. Hill, L. Perelman, and A. Adcroft, 1997b: Hydrostatic, quasi-hydrostatic, and nonhydrostatic ocean modeling. *J. Geophys. Res.*, **102**, 5733–5752, doi:10.1029/96JC02776.

McDougall, T. J., D. R. Jackett, D. G. Wright, and R. Feistel, 2003: Accurate and computationally efficient algorithms for potential temperature and density of seawater. *J. Atmos. Oceanic Technol.*, **20**, 730–741, doi:10.1175/1520-0426(2003)20<730:AACEAF>2.0.CO;2.

Mechoso, C. R., 1980: Baroclinic instability of flows along sloping boundaries. *J. Atmos. Sci.*, **37**, 1393–1399, doi:10.1175/1520-0469(1980)037<1393:BIOFAS>2.0.CO;2.

Muench, R. D., and A. L. Gordon, 1995: Circulation and transport of water along the western Weddell Sea margin. *J. Geophys. Res.*, **100**, 18 503–18 515, doi:10.1029/95JC00965.

Munday, D. R., and X. Zhai, 2013: Modulation of eddy kinetic energy, temperature variance, and eddy heat fluxes by surface buoyancy forcing. *Ocean Modell.*, **62**, 27–38, doi:10.1016/j.ocemod.2012.11.003.

Nakayama, Y., K. I. Ohshima, Y. Matsumura, Y. Fukamachi, and H. Hasumi, 2014: A numerical investigation of formation and variability of Antarctic Bottom Water off Cape Darnley, East

Antarctica. *J. Phys. Oceanogr.*, **44**, 2921–2937, doi:10.1175/JPO-D-14-0069.1.

Newsom, E. R., C. M. Bitz, F. O. Bryan, R. Abernathey, and P. R. Gent, 2016: Southern Ocean deep circulation and heat uptake in a high-resolution climate model. *J. Climate*, **29**, 2597–2619, doi:10.1175/JCLI-D-15-0513.1.

Nicholls, K. W., S. Østerhus, K. Makinson, T. Gammelsrød, and E. Fahrbach, 2009: Ice-ocean processes over the continental shelf of the southern Weddell Sea, Antarctica: A review. *Rev. Geophys.*, **47**, RG3003, doi:10.1029/2007RG000250.

Nøst, O. A., M. Biuw, V. Tverberg, C. Lydersen, T. Hattermann, Q. Zhou, L. H. Smedsrud, and K. M. Kovacs, 2011: Eddy overturning of the Antarctic Slope Front controls glacial melting in the eastern Weddell Sea. *J. Geophys. Res.*, **116**, C11014, doi:10.1029/2011JC006965.

Ohshima, K. I., and Coauthors, 2013: Antarctic Bottom Water production by intense sea-ice formation in the Cape Darnley polynya. *Nat. Geosci.*, **6**, 235–240, doi:10.1038/ngeo1738.

Orsi, A. H., S. S. Jacobs, A. L. Gordon, and M. Visbeck, 2001: Cooling and ventilating the abyssal ocean. *Geophys. Res. Lett.*, **28**, 2923–2926, doi:10.1029/2001GL012830.

Ou, H.-W., 2007: Watermass properties of the Antarctic Slope Front: A simple model. *J. Phys. Oceanogr.*, **37**, 50–59, doi:10.1175/JPO2981.1.

Padman, L., S. L. Howard, A. H. Orsi, and R. D. Muench, 2009: Tides of the northwestern Ross Sea and their impact on dense outflows of Antarctic Bottom Water. *Deep-Sea Res. II*, **56**, 818–834, doi:10.1016/j.dsr2.2008.10.026.

Park, Y.-H., E. Charriaud, and M. Fieux, 1998: Thermohaline structure of the Antarctic surface water/winter water in the Indian sector of the Southern Ocean. *J. Mar. Syst.*, **17**, 5–23, doi:10.1016/S0924-7963(98)00026-8.

Pennel, R., A. Stegner, and K. Béranger, 2012: Shelf impact on buoyant coastal current instabilities. *J. Phys. Oceanogr.*, **42**, 39–61, doi:10.1175/JPO-D-11-016.1.

Plumb, R. A., and R. Ferrari, 2005: Transformed Eulerian-mean theory. Part I: Nonquasigeostrophic theory for eddies on a zonal-mean flow. *J. Phys. Oceanogr.*, **35**, 165–174, doi:10.1175/JPO-2669.1.

Prather, M. J., 1986: Numerical advection by conservation of second-order moments. *J. Geophys. Res.*, **91**, 6671–6681, doi:10.1029/JD091iD06p06671.

Purkey, S. G., and G. C. Johnson, 2013: Antarctic Bottom Water warming and freshening: Contributions to sea level rise, ocean freshwater budgets, and global heat gain. *J. Climate*, **26**, 6105–6122, doi:10.1175/JCLI-D-12-00834.1.

Rhines, P. B., 1975: Waves and turbulence on a beta-plane. *J. Fluid Mech.*, **69**, 417–443, doi:10.1017/S0022112075001504.

——, 1994: Jets. *Chaos*, **4**, 313–339, doi:10.1063/1.166011.

Rignot, E., and S. S. Jacobs, 2002: Rapid bottom melting widespread near Antarctic Ice Sheet grounding lines. *Science*, **296**, 2020–2023, doi:10.1126/science.1070942.

Schmidt, G. A., C. M. Bitz, U. Mikolajewicz, and L.-B. Tremblay, 2004: Ice–ocean boundary conditions for coupled models. *Ocean Modell.*, **7**, 59–74, doi:10.1016/S1463-5003(03)00030-1.

Skinner, L., S. Fallon, C. Waelbroeck, E. Michel, and S. Barker, 2010: Ventilation of the deep Southern Ocean and deglacial CO_2 rise. *Science*, **328**, 1147–1151, doi:10.1126/science.1183627.

Spall, M. A., 2013: Dense water formation around islands. *J. Geophys. Res. Oceans*, **118**, 2507–2519, doi:10.1002/jgrc.20185.

Spence, P., S. M. Griffies, M. H. England, A. M. Hogg, O. A. Saenko, and N. C. Jourdain, 2014: Rapid subsurface warming and circulation changes of Antarctic coastal waters by poleward shifting winds. *Geophys. Res. Lett.*, **41**, 4601–4610, doi:10.1002/2014GL060613.

Stern, A., L.-P. Nadeau, and D. Holland, 2015: Instability and mixing of zonal jets along an idealized continental shelf break. *J. Phys. Oceanogr.*, **45**, 2315–2338, doi:10.1175/JPO-D-14-0213.1.

Stewart, A. L., and A. F. Thompson, 2012: Sensitivity of the ocean's deep overturning circulation to easterly Antarctic winds. *Geophys. Res. Lett.*, **39**, L18604, doi:10.1029/2012GL053099.

——, and ——, 2013: Connecting Antarctic cross-slope exchange with Southern Ocean overturning. *J. Phys. Oceanogr.*, **43**, 1453–1471, doi:10.1175/JPO-D-12-0205.1.

——, and ——, 2015a: Eddy-mediated transport of warm circumpolar deep water across the Antarctic Shelf Break. *Geophys. Res. Lett.*, **42**, 432–440, doi:10.1002/2014GL062281.

——, and ——, 2015b: The neutral density temporal residual mean overturning circulation. *Ocean Modell.*, **90**, 44–56, doi:10.1016/j.ocemod.2015.03.005.

——, R. Ferrari, and A. F. Thompson, 2014: On the importance of surface forcing in conceptual models of the deep ocean. *J. Phys. Oceanogr.*, **44**, 891–899, doi:10.1175/JPO-D-13-0206.1.

St-Laurent, P., J. M. Klinck, and M. S. Dinniman, 2013: On the role of coastal troughs in the circulation of warm circumpolar deep water on Antarctic shelves. *J. Phys. Oceanogr.*, **43**, 51–64, doi:10.1175/JPO-D-11-0237.1.

Su, Z., A. L. Stewart, and A. F. Thompson, 2014: An idealized model of Weddell Gyre export variability. *J. Phys. Oceanogr.*, **44**, 1671–1688, doi:10.1175/JPO-D-13-0263.1.

Tamura, T., K. I. Ohshima, and S. Nihashi, 2008: Mapping of sea ice production for Antarctic coastal polynyas. *Geophys. Res. Lett.*, **35**, L07606, doi:10.1029/2007GL032903.

Taylor, G. I., 1922: Diffusion by continuous movements. *Proc. London Math. Soc.*, **s2-20**, 196–212, doi:10.1112/plms/s2-20.1.196.

Thompson, A. F., 2010: Jet formation and evolution in baroclinic turbulence with simple topography. *J. Phys. Oceanogr.*, **40**, 257–278, doi:10.1175/2009JPO4218.1.

——, and K. J. Heywood, 2008: Frontal structure and transport in the northwestern Weddell Sea. *Deep-Sea Res. I*, **55**, 1229–1251, doi:10.1016/j.dsr.2008.06.001.

——, and A. C. Naveira Garabato, 2014: Equilibration of the Antarctic Circumpolar Current by standing meanders. *J. Phys. Oceanogr.*, **44**, 1811–1828, doi:10.1175/JPO-D-13-0163.1.

——, K. J. Heywood, S. Schmidtko, and A. L. Stewart, 2014: Eddy transport as a key component of the Antarctic overturning circulation. *Nat. Geosci.*, **7**, 879–884, doi:10.1038/ngeo2289.

Tréguier, A.-M., and J. C. McWilliams, 1990: Topographic influences on wind-driven, stratified flow in a β-plane channel: An idealized model for the Antarctic Circumpolar Current. *J. Phys. Oceanogr.*, **20**, 321–343, doi:10.1175/1520-0485(1990)020<0321:TIOWDS>2.0.CO;2.

Uotila, J., T. Vihma, and J. Launiainen, 2000: Response of the Weddell Sea pack ice to wind forcing. *J. Geophys. Res.*, **105**, 1135–1151, doi:10.1029/1999JC900265.

Vallis, G. K., 2006: *Atmospheric and Oceanic Fluid Dynamics: Fundamentals* and *Large-Scale Circulation*. Cambridge University Press, 745 pp.

——, and M. E. Maltrud, 1993: Generation of mean flows and jets on a beta plane and over topography. *J. Phys. Oceanogr.*, **23**, 1346–1362, doi:10.1175/1520-0485(1993)023<1346:GOMFAJ>2.0.CO;2.

Visbeck, M., J. Marshall, T. Haine, and M. Spall, 1997: Specification of eddy transfer coefficients in coarse-resolution ocean circulation models. *J. Phys. Oceanogr.*, **27**, 381–402, doi:10.1175/1520-0485(1997)027<0381:SOETCI>2.0.CO;2.

Wang, Q., S. Danilov, E. Fahrbach, J. Schröter, and T. Jung, 2012: On the impact of wind forcing on the seasonal variability of Weddell Sea Bottom Water transport. *Geophys. Res. Lett.*, **39**, L06603, doi:10.1029/2012GL051198.

Ward, M. L., and A. M. Hogg, 2011: Establishment of momentum balance by form stress in a wind-driven channel. *Ocean Modell.*, **40**, 133–146, doi:10.1016/j.ocemod.2011.08.004.

Williams, P. D., and C. W. Kelsall, 2015: The dynamics of baroclinic zonal jets. *J. Atmos. Sci.*, **72**, 1137–1151, doi:10.1175/JAS-D-14-0027.1.

Zhang, Y., J. Pedlosky, and G. R. Flierl, 2011: Cross-shelf and out-of-bay transport driven by an open-ocean current. *J. Phys. Oceanogr.*, **41**, 2168–2186, doi:10.1175/JPO-D-11-08.1.

Zhou, Q., T. Hattermann, O. A. Nøst, M. Biuw, K. M. Kovacs, and C. Lydersen, 2014: Wind-driven spreading of fresh surface water beneath ice shelves in the eastern Weddell Sea. *J. Geophys. Res. Oceans*, **119**, 3818–3833, doi:10.1002/2013JC009556.